

Metadamping: Dissipation Emergence in Elastic Metamaterials

Clémence L. Bacquet*, Hasan Al Ba'ba'a[†], Michael J. Frazier[‡],
Mostafa Nouh[†], Mahmoud I. Hussein^{*,1}

*Ann and H.J. Smead Department of Aerospace Engineering Sciences, University of Colorado Boulder, Boulder, CO, United States

[†]Department of Mechanical and Aerospace Engineering, State University of New York at Buffalo, Buffalo, NY, United States

[‡]Department of Mechanical and Aerospace Engineering, University of California San Diego, San Diego, CA, United States

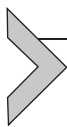
¹Corresponding author: e-mail address: mih@colorado.edu

Contents

1. Phononic Materials: Dynamical Design at the Material Level	116
1.1 Material Dynamics	116
1.2 Consideration of Material Damping	119
2. Metadamping: Damping Emergence	125
2.1 Locally Resonant Metamaterials	125
2.2 Metadamping in Locally Resonant Metamaterials	125
3. Unconventional Metamaterial Designs	130
3.1 Nonlocal Metamaterial Design	131
3.2 Dispersion Characteristics and Transitions	132
4. Static Equivalence at the Long-Wave Speed Limit	137
5. Metadamping in Nonlocal Metamaterials	139
6. Parametric Study of Metadamping	143
7. Effect of Core Damping Model	147
7.1 Viscoelasticity: Background and Modeling	147
7.2 Metadamping in Viscoelastic Phononic Materials	150
8. Experimental Validation of Metadamping	153
8.1 Pillared Beam: One-Dimensional Metamaterial	154
8.2 Evidence of Metadamping	156
8.3 Effect of Added Mass on Dissipation	159
9. Conclusions	160
Acknowledgments	161
References	161

Abstract

Resonant elastic metamaterials are artificial material systems that exhibit unique dynamical properties shaped by the intrinsic interaction between resonances and traveling dispersive waves. In this chapter, we provide a technical review of the recently proposed concept of dissipation emergence in elastic metamaterials. This concept is termed “metadamping.” Unlike conventional materials used to dampen vibrations where the damping capacity is affected by the atomic configuration, defects, and/or rheological properties, here the level of dissipation is controlled via the dynamics of the metamaterial’s resonant substructures. In this manner, it is possible to create a net material system that is both stiff and highly damped, to absorb vehicle vibrations for example. The chapter starts with a motivation and introduction of metadamping, and then presents an in-depth analysis and parametric study of metadamping in the context of both locally and nonlocally resonant elastic metamaterials modeled as mass-spring-dashpot systems. The effect of the core damping model (e.g., viscous vs nonviscous) is also examined. Finally, a review is given of metadamping in a pillared beam that has recently been investigated by experiments, simulations, and theory.



1. PHONONIC MATERIALS: DYNAMICAL DESIGN AT THE MATERIAL LEVEL

1.1 Material Dynamics

The observed properties of materials—acoustic, mechanical, etc.—are the cumulative result of many small-scale processes and interactions occurring within the material microstructure. Many technological applications require extraordinary materials that satisfy exceptional demands. Thus, the ability to tailor the microstructure and, consequently, the material behavior for applications is desirable. Chemistry represents a conventional avenue for manipulating the microstructure at the atomic/molecular/grain-boundary scale to achieve the desired material performance. Alternatively, especially with the advent of additive manufacturing technology, the internal structure may be designed and implemented at the *macroscopic* level to elicit unique, even counterintuitive, performance from the resulting architected material—with the possibility of extending the frontier of material behavior. Here, we focus on the dynamical aspects of such materials, termed *phononic materials*, which include phononic crystals (PC) and acoustic/elastic metamaterials (Kushwaha, Halevi, Dobrzynski, & Djafari-Rouhani, 1993; Liu et al., 2000; Sigalas & Economou, 1992). And in particular, we focus on the recently proposed concept of *metadamping* which allows us to design the material architecture in a way that renders it more dissipative than the nominal case without such architecture (Hussein & Frazier, 2013b).

To confine the discussion to within a manageable scope, we examine here only a sample of their physics and potential utility.

Phononic materials, generally, emerge from the periodic arrangement of small-scale building blocks—reminiscent of molecules in natural crystals—which, through scattering/interference and/or resonance phenomena, act to control the propagation of acoustic/elastic plane waves. Fundamentally, over specific frequency ranges, i.e., the *pass bands*, a phononic material is transparent to vibrational plane waves, which propagate at different speeds in contrast to the constant sonic speeds of many nondispersive conventional materials. Outside these frequency bands, i.e., within the *stop bands* or *band gaps*, the material internal structure scatters and/or localizes the wave energy, prohibiting transmission in all or specific directions. Waveguides and acoustic filters are two basic applications of this behavior. However, through careful design of building blocks forming the material's internal structure, the unique dynamics of phononic materials may be exploited in a myriad of original applications [e.g., flat acoustic lenses (Yang et al., 2004; Zhang & Liu, 2004), acoustic/elastic cloaks (Brun, Guenneau, & Movchan, 2009; Cummer & Schurig, 2007), phononic subsurfaces for flow control (Hussein, Biringen, Bilal, & Kucala, 2015), to name a few] (Deymier, 2013; Hussein, Leamy, & Ruzzene, 2014; Khelif & Adibi, 2015; Laude, 2015; Phani & Hussein, 2017).

One of the earliest and simplest examples of a phononic material is the one-dimensional medium composed of periodically alternating layers of differing composition—mass-density and elasticity—such as shown in Fig. 1A (Kohn, Krumhansl, & Lee, 1972; Lee & Yang, 1973; Sun, Achenbach, & Herrmann, 1968). Within a homogeneous medium, a vibrational wave of arbitrary frequency ω , and wavenumber (i.e., spatial frequency) κ , propagates at a constant speed, $c_0 = \omega/\kappa$. As can be seen in Fig. 1A, within a phononic material, waves of different frequencies travel at different speeds—a phenomenon referred to as *dispersion*—indicative of a nonlinear relationship between ω and κ . For the layered medium, this is accommodated by the superposition of waves transmitted and reflected at the layer interfaces. Moreover, over specific frequency ranges, the scattering/interference is sufficient to prevent the associated waves from propagating within the material. Fig. 1C illustrates each of these scenarios where the displacement profiles are plotted over several unit cells, the fundamental repeating structure. Within the pass band, the wave propagates through the phononic material such that the displacement profile encompasses the entire—theoretically infinite—domain. In contrast, within the band

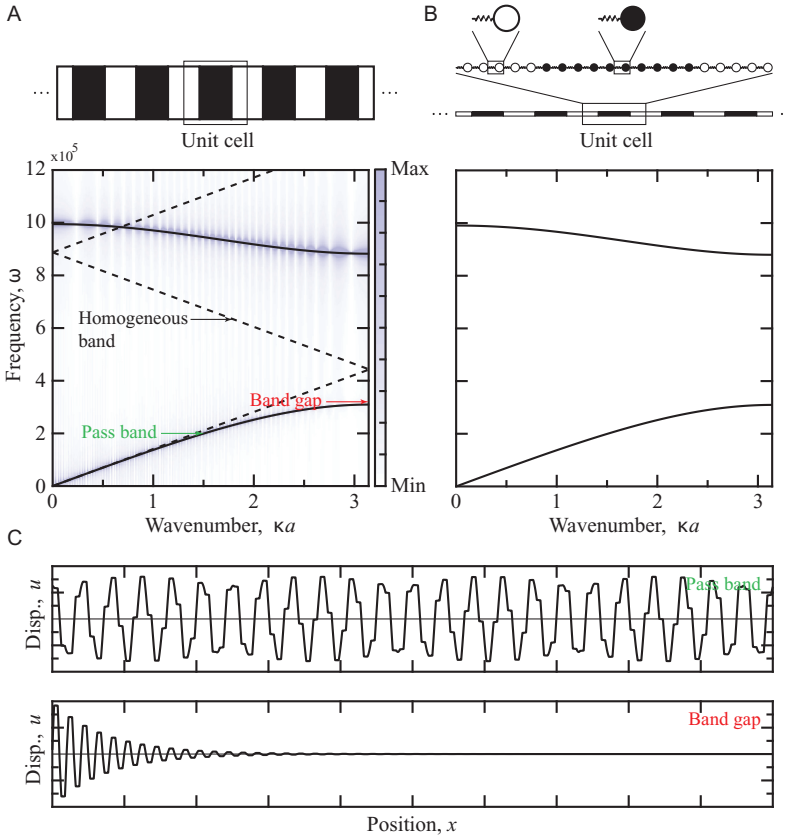


Fig. 1 (A) Dispersion diagram of a layered medium (continuous model) as determined from numerical and analytical treatments. (B) Dispersion diagram of a mass-spring system (discrete model) determined analytically. (C) Displacement profile in corresponding finite layered medium at different frequencies illustrating the contrast in response between the pass band (top) and band gap (bottom) cases.

gap, the wave amplitude decays with distance and the displacement nodes remain fixed in space for all time.

In Fig. 1A, we present the results of simulation and analytics. For the simulation, a layered medium composed of 100 cells is disturbed by an impulse at the mid-span, producing a wide spectrum of waves that propagate away from the site of initial disturbance. Prior to reaching either end of the medium, the waves interact only with each other and the underlying material periodicity of the system, mimicking an infinite medium. Under these conditions, a Fourier transform of the displacement in space (with $e^{i\kappa x}$) and time (with $e^{-i\omega t}$) produces the density plot shown, where the narrow, darker regions identify waves with spectral characteristics (i.e., ω and κ) suitable for

transmission through the layered medium and the brighter regions represent incompatible characteristics. The color map in Fig. 1A and similar diagrams produced via simulation are instructive in revealing the dispersion properties of the relevant phononic material design but are computationally expensive, especially for two- and three-dimensional systems with complex unit-cell designs. Alternatively, the periodic arrangement of the material constituents, reminiscent of molecules in natural crystals, opens phononic materials to theoretical analysis via Floquet–Bloch theorem (henceforth simplified to Bloch) from solid-state physics. For one-dimensional elastodynamic problem, this is expressed as (Bloch, 1929; Floquet, 1883):

$$u(x, t) = \tilde{u}(x)e^{i(kx - \omega t)} \quad (1)$$

where $u(x, t)$ is the displacement. The amplitude function $\tilde{u}(x)$ has the same periodicity at the underlying medium, $x \in [0, \pm a]$ where a is the lattice spacing or unit-cell length. As a consequence, $u(x \pm na, t) = u(x, t)e^{\pm i\kappa na}$ for any arbitrary integer n , which permits the solution for $x \in (-\infty, \infty)$ to be determined from the analysis of a finite segment of material of dimension a —the unit cell. This modeling concept applies to two- and three-dimensional systems as well. By considering only a single unit cell rather than the potential myriad of cells, Bloch’s theorem greatly reduces computation demands and yields a compact, theoretical representation of the wave propagation characteristics. Fig. 1A illustrates excellent agreement between numerical (density plot) and analytical (smooth curves) results for the layered medium.

As mentioned previously, the layered medium is one of the most elementary practical representations of a phononic material which could serve as a simple demonstration. However, in what follows, we utilize simple lumped-parameter models that capture all the essential physics and make the connection between unit-cell configuration and performance more accessible. Indeed, in regard to the ability to capture the essential physics of a problem, as shown in Fig. 1B, the dispersion diagram of the corresponding lumped-parameter model closely resembles that of its continuum counterpart shown in Fig. 1A. This model uses masses and springs to represent each layer of the unit cell, with each mass and spring defined as $m = \rho AL$ and $k = EA/L$, respectively, where ρ is the density, E is the Young’s modulus, and A and L denote the rod cross-sectional area and length, respectively.

1.2 Consideration of Material Damping

Inherent to every material, damping mechanisms (e.g., friction) dissipate the wave energy, affecting the propagation and spatial attenuation characteristics

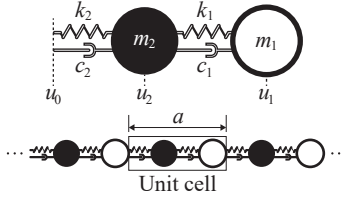


Fig. 2 Discrete model of a phononic material constructed from a unit cell of two interacting masses which repeats infinitely along one dimension.

(Crandall, 1970). However, damping is often unaccounted for in theoretical analysis, removing a practical aspect of material performance and a mean to control that performance. In the following, we discuss the physics and utility of damping in phononic materials [for further reading, see, e.g., Hussein (2009b), Hussein and Frazier (2010), Frazier and Hussein (2016), Al Ba'ba'a and Nouh (2017)]. To this end, we primarily use the mass-spring-damper model shown in Fig. 2, which forms the basis of one-dimensional phononic material similar to the discrete example discussed previously.

The set of equations that describe the motion of each degree of freedom in the unit cell are collected in matrix form as [see Hussein and Frazier (2013a) and Frazier and Hussein (2016) for the derivations]

$$\mathbf{M}\ddot{\mathbf{u}} + \mathbf{C}\dot{\mathbf{u}} + \mathbf{K}\mathbf{u} = \mathbf{f} \quad (2)$$

where the mass \mathbf{M} , viscous damping \mathbf{C} , and stiffness \mathbf{K} matrices are, respectively, given by

$$\mathbf{M} = m_2 \begin{bmatrix} 1/r_m & 0 & 0 \\ 0 & 1 & 0 \\ 0 & 0 & 0 \end{bmatrix} \quad (3a)$$

$$\mathbf{C} = c_2 \begin{bmatrix} 1/r_c & -1/r_c & 0 \\ -1/r_c & 1/r_c + 1 & -1 \\ 0 & -1 & 1 \end{bmatrix} \quad (3b)$$

$$\mathbf{K} = k_2 \begin{bmatrix} 1/r_k & -1/r_k & 0 \\ -1/r_k & 1/r_k + 1 & -1 \\ 0 & -1 & 1 \end{bmatrix} \quad (3c)$$

consistent with the displacement degrees of freedom $\mathbf{u}^T = [u_1 \ u_2 \ u_0]$. The superposed dot represents differentiation with respect to time. The forces

applied by neighboring cells are organized in $\mathbf{f}^T = [f_1 f_2 f_0]$. Here, we introduce the material property relations $r_m = m_2/m_1$, $r_c = c_2/c_1$, $r_k = k_2/k_1$. Note, Eq. (2) represents the equation of motion of a single unit cell viewed as a finite entity. To model the dynamics of the corresponding infinite, periodic medium, we apply Bloch boundary conditions which establish a relationship (perpetuating in space ad infinitum) between the unit-cell boundary states and those of its neighbors. We define a condensed displacement vector containing only the essential degrees of freedom, that is, the internal and essential boundary displacement, $\hat{\mathbf{u}}^T = [u_1 u_2]$. From Bloch's theorem, $u_0 = u_1 e^{-i\kappa a}$. Thus, the condensed and full set of displacement degrees of freedom are related via the transformation, \mathbf{T} , as follows

$$\mathbf{u} = \mathbf{T}\hat{\mathbf{u}} = \begin{bmatrix} 1 & 0 \\ 0 & 1 \\ e^{-i\kappa a} & 0 \end{bmatrix} \begin{bmatrix} u_1 \\ u_2 \end{bmatrix}. \quad (4)$$

When applied to the equation of motion, the transformation yields

$$\hat{\mathbf{M}}\ddot{\hat{\mathbf{u}}} + \hat{\mathbf{C}}\dot{\hat{\mathbf{u}}} + \hat{\mathbf{K}}\hat{\mathbf{u}} = \mathbf{0} \quad (5)$$

with $\hat{\mathbf{M}} = \mathbf{T}^H \mathbf{M} \mathbf{T}$, $\hat{\mathbf{C}} = \mathbf{T}^H \mathbf{C} \mathbf{T}$, and $\hat{\mathbf{K}} = \mathbf{T}^H \mathbf{K} \mathbf{T}$, where the superscript ‘‘H’’ represents the complex transpose operation. Given that Bloch analysis is concerned with free wave motion, we set $\mathbf{T}^H \mathbf{f} = \mathbf{0}$.

From a theoretical perspective, the wave frequency is often assumed to be strictly real-valued regardless of the damping condition (Castanier & Pierre, 1993; Collet, Ouisse, Ruzzene, & Ichchou, 2011; Farzbod & Leamy, 2011; Langley, 1994a; Mead, 1973; Merheb et al., 2008; Moiseyenko & Laude, 2011). Consequently, according to Eq. (1), wave attenuation (due to interference and/or damping) may only occur over the propagation distance as the wavenumber is free to be complex-valued, $\kappa = \kappa_R + i\kappa_I$. This may be considered the controlled laboratory perspective, that is, the material response is what may be expected when exciting an extended, but finite, structure at the boundary at a prescribed frequency; hence supplying continuous injection of wave energy. However, if we are interested in the inherent material response following an initial input of energy, our analysis of wave propagation in damped phononic materials allows the temporal frequency to be complex. In this context, waves attenuate in space (due to scattering/interference and resonance) and time (due to material damping). This may be considered the free-motion perspective as the dynamics stem purely from the response of the material to an initial disturbance, as opposed to a sustained external

stimulation. In the absence of damping, the two approaches are equivalent. Damping reveals the unique dynamics of each operation condition, and in principle it is possible to solve for an all-complex band structure where both the frequencies and wavenumbers are complex (Frazier & Hussein, 2016; Hussein, Frazier, & Abedinnassab, 2013). For real-valued frequencies, the band-gap effect is unadulterated only in the complete absence of damping (not seen in practice), otherwise, the band gap closes with the slightest level of damping. Conversely, for complex-valued frequencies, the impact of wave interferences is more intact and the band gap remains complete except under extreme conditions (Frazier & Hussein, 2016; Phani & Hussein, 2013).

For general free wave motion, the displacement solution varies according to $e^{\lambda t}$ where λ is the complex frequency whose real and imaginary components are to be determined. Modifying Bloch's theorem accordingly and subsequently applying the derivatives in Eq. (2) yields the following quadratic eigenvalue problem in λ

$$(\lambda^2 \hat{\mathbf{M}} + \lambda \hat{\mathbf{C}} + \hat{\mathbf{K}}) \hat{\mathbf{u}} = \mathbf{0} \quad (6)$$

Here we can utilize the state-space transformation from structural dynamics (Wagner & Adhikari, 2003) to formulate an eigenvalue problem with twice the degrees of freedom but linear in construction (Frazier & Hussein, 2015; Hussein & Frazier, 2010, 2013a). We define the state vector, $\hat{\mathbf{y}}^T = [\dot{\hat{\mathbf{u}}} \quad \hat{\mathbf{u}}]$, enabling the state-space transformation

$$\begin{bmatrix} \mathbf{0} & \hat{\mathbf{M}} \\ \hat{\mathbf{M}} & \hat{\mathbf{C}} \end{bmatrix} \dot{\hat{\mathbf{y}}} + \begin{bmatrix} -\hat{\mathbf{M}} & \mathbf{0} \\ \mathbf{0} & \hat{\mathbf{K}} \end{bmatrix} \hat{\mathbf{y}} = \mathbf{0} \quad (7)$$

Assuming the time-dependence of the state vector is also of the form $e^{\lambda t}$, we formulate the following generalized linear eigenvalue problem in λ

$$\left(\lambda \begin{bmatrix} \mathbf{0} & \hat{\mathbf{M}} \\ \hat{\mathbf{M}} & \hat{\mathbf{C}} \end{bmatrix} + \begin{bmatrix} -\hat{\mathbf{M}} & \mathbf{0} \\ \mathbf{0} & \hat{\mathbf{K}} \end{bmatrix} \right) \hat{\mathbf{y}} = \mathbf{0} \quad (8)$$

In general, the complex eigenvalues take the form

$$\lambda(\kappa) = -\xi(\kappa)\omega_r(\kappa) \pm i\omega_d(\kappa) \quad (9)$$

Inserting Eq. (9) into $e^{\lambda t}$, it is apparent that $\omega_d(\kappa)$, the damped wave frequency, leads to temporal oscillations and $\xi(\kappa)\omega_r(\kappa)$ is responsible for the decay of the wave amplitude over time. Specifically, the quantity $\xi(\kappa)$ is the dimensionless damping ratio (loss factor) and $\omega_r(\kappa)$ is termed the

“resonant frequency.” The wavenumber-dependent damping ratio relation is extracted from the complex eigenvalues as follows

$$\xi(\kappa) = -\frac{\text{Re}[\lambda(\kappa)]}{|\lambda(\kappa)|} \quad (10)$$

Naturally, in the absence of damping, $\xi(\kappa) = 0$ and $\omega_d(\kappa)$ is identical to the undamped solution $\omega(\kappa)$. In addition, due to the method of extraction, the maximum value that $\xi(\kappa)$ may attain over a range of wavenumbers is unity, which requires that $\omega_d(\kappa) = 0$ over the corresponding κ range.

Fig. 3A and B shows the damped frequency and damping ratio dispersion diagrams for specific normalized damping intensities β/ω_0 , including the undamped scenario $\beta/\omega_0 = 0$ for reference. The ratio $\beta = c_2/m_2$ is a measure of the damping intensity and $\omega_0^2 = k_2/m_2$ is the natural frequency of the oscillator m_2 . The specific material property ratios selected for this example are $r_m = 3$, $r_c = 1/2$, $r_k = 1$, and $\omega_0 = 65.32$ rad/s. Notice that viscous damping compacts the frequency band structure, affecting higher frequencies more acutely than lower ones. This is corroborated by the corresponding damping ratios in Fig. 3B which expand as the damping intensity increases, most rapidly for wavenumbers corresponding to higher frequencies. In the extreme, we can observe two intriguing phenomena not encountered in real-frequency analysis: band overtaking and band cut-off (Hussein, 2009b; Hussein & Frazier, 2010; Phani & Hussein, 2013). Band overtaking occurs when frequency bands cross; band cut-off describes the scenario in which frequency bands do not span the full range of wavenumbers. In Fig. 3A, we observe a case of band overtaking at $\beta/\omega_0 = 0.45$. In particular, we observe that the upper band (dashed) drops at a much faster rate than the lower band (solid) as the corresponding damping ratio is greater, enabling the overtake. This is quantitatively illustrated by tracking the band-gap width as a function of damping intensity, as illustrated in Fig. 3C. In some cases, if the overtake takes place on an upper band, a band gap can decrease in width more abruptly (Hussein, 2009b).

In Fig. 3A, we observe that when the level of damping exceeds a certain value, the lower band gets cut-off in the wavenumber domain, i.e., it does not span the entire first irreducible Brillouin zone (IBZ), $\kappa a \in [0, \pm\pi]$. Moreover, since the upper band eventually disappears we get a wavenumber band gap, i.e., a wavenumber range where waves are prohibited from propagation. This phenomenon is analogous to the well-known concept of a

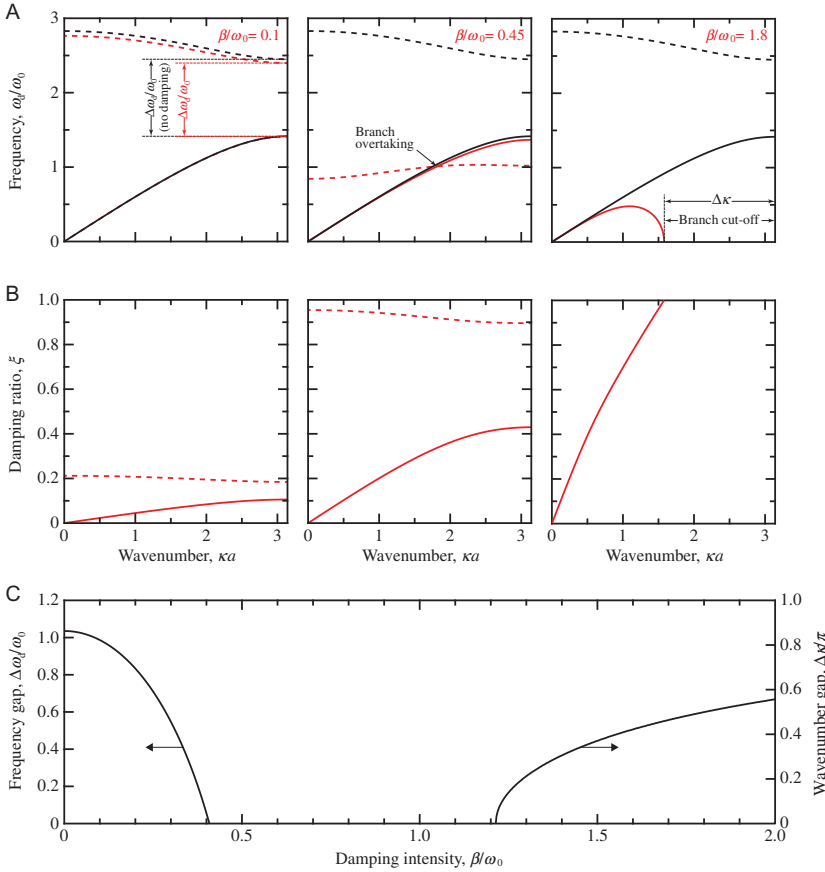


Fig. 3 (A) Dispersion diagram for the phononic crystal shown in Fig. 2 illustrating the dynamic response of the material to various damping levels: undamped, $\beta = 0$ (black) and damped, $\beta > 0$ (red). In particular, the descent of frequency bands with increased damping is highlighted, ultimately resulting in branch overtaking and band cut-off. (B) The corresponding damping ratio diagram which is unique to complex frequencies and is a measure of how rapidly the wave amplitude decays—no propagation is possible for $\xi(\kappa) \geq 1$. (C) As damping increases, the frequency bands collapse with higher frequencies outpacing lower ones, narrowing and ultimately closing the band gap and initiating band overtaking. Subsequently, beginning with higher frequency bands, a gap in the wavenumber spectrum opens, resulting in band cut-off.

frequency band gap. The damping-induced band-overtaking and band cut-off phenomena clearly present opportunities for design, building on already existing methodologies at the unit-cell level and/or a combination of the unit-cell and structural levels. However, both phenomena require substantial levels of prescribed damping.



2. METADAMPING: DAMPING EMERGENCE

2.1 Locally Resonant Metamaterials

In the previous section, we investigated the dynamics of phononic materials with and without the influence of damping; however, the continuous and discrete examples studied thus far have been of the phononic crystal type. The unit-cell structure of a PC interacts with traveling elastic waves to promote interferences, opening up band gaps. As a result, there is a dependency on unit-cell size to open band gaps.

Over the past two decades, metamaterials, whose extraordinary dynamic and mechanical properties originate from a uniquely tailored internal architecture, have spurred research in the acoustics (Liu et al., 2000), electromagnetics (Pendry, Holden, Robbins, & Stewart, 1999; Smith, Padilla, Vier, Nemat-Nasser, & Schultz, 2000), and, more recently, mechanics (Christensen, Kadic, Kraft, & Wegener, 2015) fields. Among the most intriguing applications is the possibility of a perfect lens (Pendry, 2000). Returning to our interest in the dynamical aspects of phononic materials, much of the remarkable properties of metamaterials, such as negative effective mass/density, elastic/bulk modulus, refractive index, etc.—are often the homogenized manifestation of subwavelength resonances engineered into each unit cell. These resonating bodies act to localize (rather than scatter/reflect) the wave energy to open band gaps and may take the form of heavy, elastically coated spheres in an epoxy matrix (Liu et al., 2000), pillars (Bilal & Hussein, 2013; Pennec, Djafari-Rouhani, Larabi, Vasseur, & Ladky-Hennion, 2008; Wu, Huang, Tsai, & Wu, 2008), voids in an epoxy matrix (Wang, Wen, Wen, Shao, & Liu, 2004), localized oscillators distributed along a rod (Al Ba’ba’a & Nouh, 2017; Khajehtourian & Hussein, 2014), among other possibilities. In the following, we investigate the utility of locally resonant metamaterials in addressing a long-standing materials challenge involving damping.

2.2 Metadamping in Locally Resonant Metamaterials

A variety of applications demand materials with simultaneously high damping (i.e., vibration/shock suppression) and mechanical stiffness (i.e., load-bearing capability); however, for traditional materials, a gain in one is often at the expense of the other. Consider the load-bearing and damping properties of steel and rubber as one of many such material comparisons (see Fig. 4). Following a “best-of-both-worlds” approach, even composites

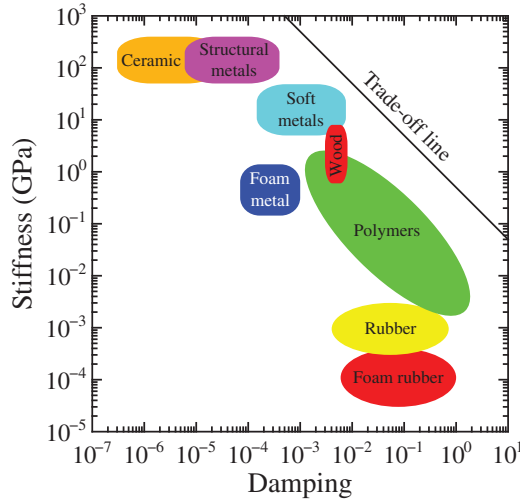


Fig. 4 Ashby chart of stiffness vs damping of common materials illustrating the stiffness-damping trade-off.

composed of stiff and damped constituents are compelled by inherent properties and filling fraction trade-off to sacrifice one property to promote the other.

In addition to their previously mentioned attributes and applications in the absence of material damping, metamaterials may exhibit a greater capacity for wave attenuation than traditional, nonarchitected materials and PCs when damping is taken into account. This gives metamaterials the potential to enable very high levels of dissipation with sustained load-bearing capacity. This emergent damping capacity, termed *metadamping* (Hussein & Frazier, 2013b), applies across a broad spectrum rather than a narrow set of frequencies and has been demonstrated in metamaterials supporting monopolar (Frazier & Hussein, 2015) and dipolar (Frazier & Hussein, 2015; Hussein & Frazier, 2013b) resonances, and resonances in more complex configurations (Antoniadis, Chronopoulos, Spitas, & Koulocheris, 2015; DePauw, Al Ba'ba'a, & Nouh, 2018). In the following, we illustrate the metadamping phenomenon, beginning with metamaterials based on local resonance and then through other architectures.

Fig. 5 shows the initial three material architectures to be considered. Fig. 5A is a representative phononic crystal which relies exclusively on scattering and interference between forward and backward propagating waves for its dispersive properties, notably, the band gap. Fig. 5B and C are two prototypical metamaterial designs whose dynamics are affected by local

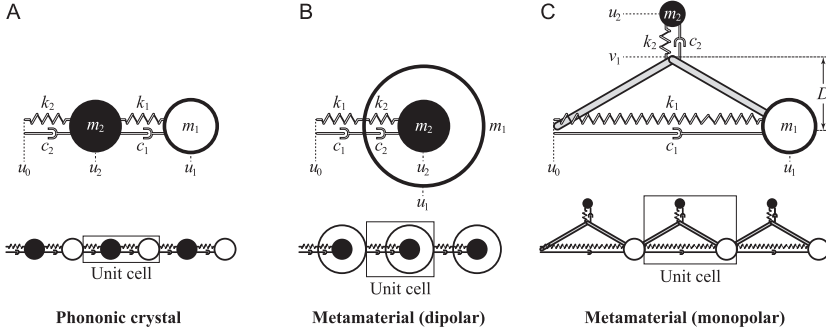


Fig. 5 Discrete models of (A) a phononic crystal (utilizing scattering and wave interferences), and (B) dipolar and (C) monopolar metamaterials (utilizing local resonance). These lumped-parameter models are simple, yet retain the essential physics of their laboratory counterparts.

resonances, particularly dipolar and monopolar, in addition to wave interference due to the periodicity. In acoustics, a monopole radiates vibrational waves equally well in all directions; thus, the truss structure in the monopole metamaterial design in Fig. 5C, which equally applies the influence of the resonator to both ends of the unit cell. A dipole consists of two monopoles of equal magnitude but opposite phase and separated by a subwavelength distance so that vibrational waves of opposite phase radiate well in two directions. This is modeled by the metamaterial unit cell in Fig. 5B. The reader is referred to the article by Russell, Titlow, and Bemmgen (1999) for more information on monopoles and dipoles.

For each metamaterial model, the equation of motion in Eq. (2) is structurally the same; however, consistent with the unique interaction among the degrees of freedom of each model, the damping and stiffness matrices are defined differently from the phononic crystal matrices introduced earlier (the mass matrix is the same). For the metamaterial with dipolar resonance, the damping and stiffness matrices become

$$\mathbf{C} = c_2 \begin{bmatrix} 1/r_c + 1 & -1 & -1/r_c \\ -1 & 1 & 0 \\ -1/r_c & 0 & 1/r_c \end{bmatrix} \quad (11a)$$

$$\mathbf{K} = k_2 \begin{bmatrix} 1/r_k + 1 & -1 & -1/r_k \\ -1 & 1 & 0 \\ -1/r_k & 0 & 1/r_k \end{bmatrix} \quad (11b)$$

For the metamaterial with monopolar resonance, they are defined as

$$\mathbf{C} = c_2 \begin{bmatrix} 1/r_c + \delta/16 & \sqrt{\delta}/4 & -(1/r_c + \delta/16) \\ \sqrt{\delta}/4 & 1 & -\sqrt{\delta}/4 \\ -(1/r_c + \delta/16) & -\sqrt{\delta}/4 & 1/r_c + \delta/16 \end{bmatrix} \quad (12a)$$

$$\mathbf{K} = k_2 \begin{bmatrix} 1/r_k + \delta/16 & \sqrt{\delta}/4 & -(1/r_k + \delta/16) \\ \sqrt{\delta}/4 & 1 & -\sqrt{\delta}/4 \\ -(1/r_k + \delta/16) & -\sqrt{\delta}/4 & 1/r_k + \delta/16 \end{bmatrix} \quad (12b)$$

where $\delta = (a/D)^2$ is an additional control parameter for the monopolar resonance (a denotes the lattice spacing).

With the above construction, the three models share the same transformation matrix \mathbf{T} as the phononic crystal, which, when applied to the equation of motion, Eq. (2), gives its reduced form in terms of the essential degrees of freedom, Eq. (5).

To facilitate a proper comparison of material performance, notice that each model contains the same damping elements and number of degrees of freedom, i.e., an advantage in the form of more effective damping mechanisms and/or more interactions is not held by either model. In addition, the three models are statically equivalent, that is, they are of equal mass and effective static stiffness, $k_{\text{eff}} = c_0^2(m_1 + m_2)/a$, where c_0 is extracted from the linear portion of the undamped dispersion diagram where $c_0 \approx \omega/\kappa$ (see Section 4 for an in-depth analysis of static equivalence). This requires $k_{1,2}$ to differ between the models, however, r_k is held constant. Specifically, for the dipolar metamaterial, $\omega_0 = 46.19$ rad/s; for the monopolar metamaterial with $\delta = 1$, $\omega_0 = 23.09$ rad/s. For the present set of material parameters, $c_0 = 40$.

In Fig. 6, we compare the response of each model to a common damping intensity, $\beta/\omega_0 = 0.1$. The results show that there are shifts in the frequency band diagrams of all three models due to damping which are consistent with what was seen in Fig. 3A—greater shifts at higher frequencies corresponding to higher damping ratios. However, despite the static equivalence and equally prescribed viscous damping, we observe that, compared to the representative PC, the metamaterials exhibit higher damping ratio values (i.e., higher dissipation) across much of the wavenumber domain. This is an indication of a considerable amplification, or emergence, of dissipation in locally resonant metamaterials compared to their phononic crystal counterparts and

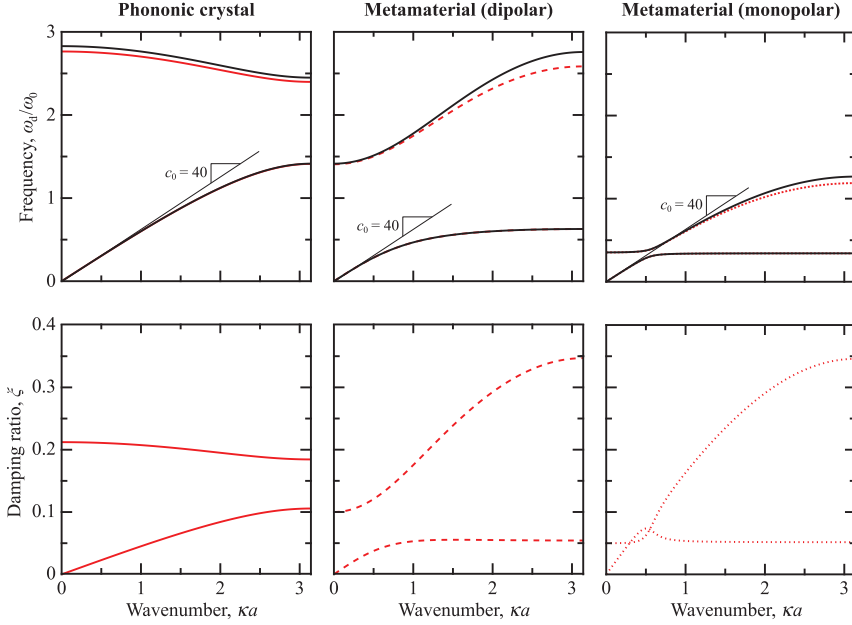


Fig. 6 Frequency and damping ratio dispersion of statically equivalent [equal mass and long-wavelength stiffness (equivalent speed of sound)] phononic crystal and metamaterial models.

showcases the effect of the internal structure design. For a more comprehensive indicator of the damping capacity of each material model, we determine the average damping ratio over the whole of the wavenumber domain and across all modes:

$$\xi_{\text{avg}} = \frac{1}{2\pi} \int_0^\pi [\xi_1(\kappa a) + \xi_2(\kappa a)] d\kappa a \quad (13)$$

The results— $\xi_{\text{avg}}^{\text{PC}} = 0.13$ for the phononic crystal, $\xi_{\text{avg}}^{\text{DP}} = 0.20$ for the dipolar metamaterial, and $\xi_{\text{avg}}^{\text{MP}} = 0.39$ for the monopolar metamaterial—reveal the superior dissipation performance of metamaterials, particularly those possessing monopolar resonances. This enhanced dissipation in metamaterials defines the metadamping phenomenon.

Fig. 7 illustrates the robustness of the metadamping phenomenon by plotting ξ_{avg} for various c_0 values. In addition, the impact of the parameter δ unique to the monopolar model is demonstrated. For the case $c_0 = 40$, even as $\delta \rightarrow 0$, monopolar metadamping still outperforms the dipolar case.

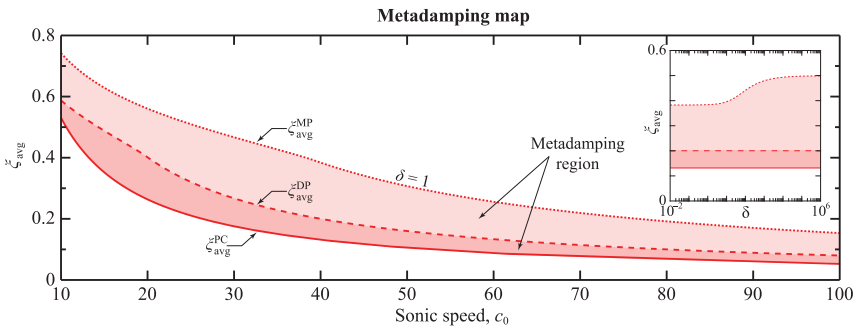
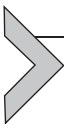


Fig. 7 Metadamping map characterizing the sonic speed dependency of the emergent increase in damping capacity in resonance-based metamaterials.

In this section, we have demonstrated the concept of metadamping theoretically due to the presence of local resonance in the internal structure of the phononic material. This finding has far reaching implications on the design of materials for numerous applications that require the reduction, mitigation, or absorption of vibrations, shock, and/or sound. While the analysis has been presented in the context of simple mass-spring-dashpot periodic chains, it can be readily extended to practical realizations of locally resonant acoustic metamaterials. Examples include material structures that utilize: heavy inclusions with compliant coatings, soft inclusions, split-resonators, inertial amplifiers, pillars, holey cylinders, and suspended masses. Other concepts for enhancing damping while retaining stiffness may be applied in conjunction with the inclusion of local resonators leading to an additive effect. While this discussion has presented metadamping as a desirable effect, an awareness and understanding of the phenomenon will aid in mitigation where it is not advantageous. Finally, while the concept of metadamping has been presented in the context of a mechanical problem, in principle it is also applicable to other disciplines in materials physics that involve both resonance and dissipation.



3. UNCONVENTIONAL METAMATERIAL DESIGNS

In pursuit of novel functionalities, unconventional metamaterial configurations have recently emerged that exhibit broader tunability of wave dispersion features and, at times, offer a pathway for physical realization of

locally resonant mechanisms (Chen, Hu, & Huang, 2017; Liu, Chan, & Sheng, 2005). The overarching theme of these novel metamaterials is the combination of phononic features and intrinsic resonators placed in unique and unprecedented configurations. Among these is the notion of resonator-to-resonator interaction with examples that range from spring-mass metamaterials with discretely coupled resonators (Hu, Tang, Das, Gao, & Liu, 2017) to elastic metamaterial beams with interconnected resonators (Beli, Arruda, & Ruzzene, 2018). In addition, other configurations feature the presence of nonlocal resonances which, rather than being confined inside an outer mass, directly interact with the preceding and following masses in a periodic chain (DePauw et al., 2018).

3.1 Nonlocal Metamaterial Design

In this section, we investigate a new class of metamaterials which comprises a nonlocal resonator and combines hybrid attributes from dipolar metamaterials (DP) and PC (DePauw et al., 2018). The new configuration—henceforth referred to as *nonlocal metamaterial* (NL)—consists of two masses m_1 and m_2 . Each two consecutive masses m_1 are connected via a spring k_1 , while each mass m_2 is sandwiched between two neighboring masses m_1 and connected to each of them via a spring k_2 , as depicted in Fig. 8. It is noted that the PC and DP configurations may be realized from the NL metamaterial configuration by setting k_1 or one of the k_2 springs equal to zero, respectively. The dashpots c_1 and c_2 are added in parallel to the respective springs in the damped case to characterize the energy dissipation in the NL metamaterial, which is capable (as will be shown later) of exercising considerably greater metadamping effects than both the PC and the DP cases with the suitable choice of parameters.

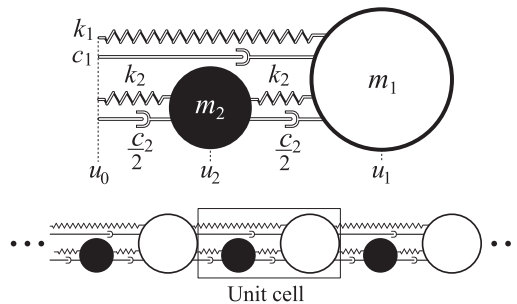


Fig. 8 Discrete model of a nonlocal metamaterial (NL) cell which repeats infinitely along one dimension.

3.2 Dispersion Characteristics and Transitions

We start by highlighting the dispersion characteristics of the undamped NL metamaterial under both free wave and driven wave conditions. In the most general form, the undamped dispersion relations are given by

$$\alpha_2 \omega^4 - \alpha_1 \omega^2 + \alpha_0 = 0 \quad (14)$$

where $\alpha_2 = m_1 m_2$ and the coefficients α_1 and α_0 for the different phononic materials are listed in Table 1.

The general dispersion relation provided in Eq. (14) depicts the free wave formulation and, for the NL case, reads

$$\omega^4 - \left(2(1 + r_m) + \frac{r_m}{r_k} \alpha \right) \omega_0^2 \omega^2 + \omega_0^4 r_m (1 + 2/r_k) \alpha = 0 \quad (15)$$

where the acoustical ω_- and optical ω_+ branches are given in closed form by

$$\omega_{\pm}^2 = \frac{\omega_0^2}{2} \left[\left(2(1 + r_m) + \frac{r_m}{r_k} \alpha \right) \pm \sqrt{\left(2(1 + r_m) + \frac{r_m}{r_k} \alpha \right)^2 - 4r_m(1 + 2/r_k)\alpha} \right] \quad (16)$$

For the free wave formulation, the dispersion curves are obtained by computing the roots of Eq. (16) over a range of $\kappa a \in [0, \pi]$ corresponding to the IBZ. Upon inspecting the results, it can be observed that the optical dispersion branch can be manipulated to exhibit a negative or positive group velocity depending on the choice of parameters, thus resembling either a PC or a resonant material, respectively. Such a feature implies the presence of a turning point where the optical branch becomes flat (i.e., $\frac{\partial \omega}{\partial \kappa} = 0$); a phenomenon that has been observed in systems with parametric amplification (Cassedy, 1967). A similar behavior has also been captured in inertially amplified locally resonant metamaterials (Al Ba'ba'a, DePauw, Singh, & Nouh, 2018). The turning point can be analytically extracted by using

Table 1 Expressions for α_0 and α_1 for Different Phononic Material ($\alpha = 2(1 - \cos \kappa a)$)

	PC	DP	MP	NL
α_0	$k_1 k_2 \alpha$	$k_1 k_2 \alpha$	$k_1 k_2 \alpha$	$k_2(2k_1 + k_2)\alpha$
α_1	$(k_1 + k_2)(m_1 + m_2)$	$k_2(m_1 + m_2) + k_1 m_2 \alpha$	$m_1 k_2 + m_2(k_1 + \frac{\delta}{16} k_2)\alpha$	$2k_2(m_1 + m_2) + k_1 m_2 \alpha$

the derivative of the dispersion relation in Eq. (15) with respect to κ (Liu & Hussein, 2012)

$$4\omega^3 \frac{\partial \omega}{\partial \kappa} - \omega_0^2 \left[2 \left(2(1+r_m) + \frac{r_m}{r_k} \alpha \right) \omega \frac{\partial \omega}{\partial \kappa} + 2a \left(\frac{r_m}{r_k} \sin \kappa a \right) \omega^2 \right] + 2a\omega_0^4 r_m (1 + 2/r_k) \sin \kappa a = 0 \quad (17)$$

Given that a flat branch dictates that $\frac{\partial \omega}{\partial \kappa} = 0$, Eq. (17) simplifies to

$$(\omega_0^2(1 + 2/r_k) - \omega^2/r_k) \sin \kappa a = 0 \quad (18)$$

which indicates that a zero group velocity exists when $\sin \kappa a = 0$ at $\kappa a = \ell \pi$, where $\ell = 0, 1, 2, \dots$, as well as for the following condition

$$\omega = \omega_0 \sqrt{2 + r_k} \quad (19)$$

Substituting Eq. (19) into Eq. (15), it can be shown that the relationship between the stiffness and mass ratios which governs the turning point of the optical branch is given by

$$r_k = 2r_m \quad (20)$$

Alternatively, the same condition associated with the turning point can be found by equating the roots of the optical branch ω_+ in Eq. (16) at $\kappa a = 0$ and $\kappa a = \pi$ (i.e., $\alpha = 0$ and $\alpha = 4$, respectively); which results in

$$\omega_+ = \omega_0 \sqrt{2(1+r_m)} \quad (21a)$$

$$\omega_+ = \omega_0 \sqrt{2r_m(1+2/r_k)} \quad (21b)$$

By equating Eqs. (21a) and (21b), the same condition to that given by Eq. (20) is found. If $2r_m > r_k$, the NL optical branch behaves in a manner consistent with resonant metamaterials while for $2r_m < r_k$, it resembles the optical branch of a PC. As a consequence, the lower and upper bounds of the resultant band gap, ω_l and ω_u , depend on whether the NL metamaterial mimics a PC or a resonant metamaterial. While ω_l can always be extracted from the dispersion solution at $\kappa a = \pi$, the value of ω_u will obviously depend on the shape of the optical branch and can correspond to the solution at either $\kappa a = 0$ or $\kappa a = \pi$. The following two equations summarize all the possible scenarios and provide comprehensive expressions for ω_l and ω_u

$$\omega_l = \min \left(\sqrt{2r_m(1+2/r_k)}, \sqrt{2} \right) \omega_0 \quad (22a)$$

$$\omega_u = \min \left(\sqrt{2(1+r_m)}, \max \left(\sqrt{2r_m(1+2/r_k)}, \sqrt{2} \right) \right) \omega_0 \quad (22b)$$

It is critical to note that when $\alpha = 4$ in Eq. (16), the acoustical branch solution can be shown to be $\omega_- = \sqrt{2}\omega_0$. It is also evident from Eqs. (22a) and (22b) that when an NL behaves like a PC, it is possible for $\sqrt{2r_m(1+2/r_k)}$ to be either greater or less than $\sqrt{2}$. In the rare occasion where $\sqrt{2r_m(1+2/r_k)} < \sqrt{2}$, this dispersion solution appears in the acoustical branch and is otherwise located in the optical branch. In cases where the upper limit $\omega_u = \sqrt{2}\omega_0$, this requires that $r_m(1+2/r_k) < 1$, which generates the following condition

$$r_m < \frac{r_k}{2+r_k} \quad (23)$$

which is a subset of the $2r_m < r_k$ case with r_m being less than unity. Interestingly, at the critical point $r_m = \frac{r_k}{2+r_k}$, the band gap of the NL metamaterial vanishes and the dispersion relation has the repeated solutions $\omega = \sqrt{2}\omega_0$ at $\kappa a = \pi$ (i.e., the discriminant of Eq. (16) becomes equal to zero). In such a case, the NL dispersion resembles that of a homogenous monatomic lattice. To summarize the previous discussion, it is concluded that one of the band-gap limits in the NL metamaterial has to be located at $\omega = \sqrt{2}\omega_0$. The different scenarios accompanying the NL dispersion relation discussed here are graphically summarized in Fig. 9.

For completeness, we also investigate the driven wave formulation which generates the wavenumber κa as an output to a prescribed frequency, i.e., $\kappa a(\omega)$. By recasting Eq. (15) in the form: $\kappa a = \cos^{-1}\Phi(\omega)$, the explicit form of the function $\Phi(\omega)$ for NL metamaterials can be written as

$$\Phi^{\text{NL}} = 1 + \frac{r_k \omega^2}{2r_m \omega_0^2} \left(\frac{\omega^2 - 2\omega_0^2(1+r_m)}{\omega_0^2(2+r_k) - \omega^2} \right) \quad (24)$$

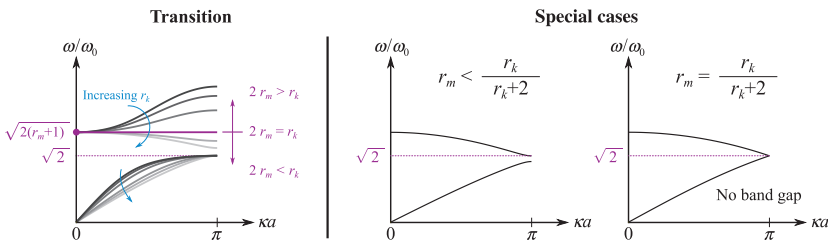


Fig. 9 Dispersion transitions in an NL metamaterial with different mass and stiffness ratios.

By inspecting Eq. (24), the presence of an antiresonance in the system can be determined from the discontinuities in the Φ^{NL} function, specifically the roots of its denominator. The NL metamaterial has an antiresonance frequency ω_R which is given by

$$\omega_R = \omega_0 \sqrt{2 + r_k} \quad (25)$$

which, as can be seen, is a function of the stiffness ratio r_k , for a given ω_0 . In addition, the driven wave problem facilitates the process of extracting the extreme points of the dispersion from the roots of $\frac{\partial \Phi^{\text{NL}}}{\partial \omega}$

$$\frac{\partial \Phi^{\text{NL}}}{\partial \omega} = \omega(\omega^4 - 2\omega_0^2(2 + r_k)\omega^2 + 2\omega_0^4(1 + r_m)(2 + r_k)) = 0 \quad (26)$$

where nonzero solutions for ω in Eq. (26) are found as

$$\hat{\omega}_{\pm} = \omega_0 \sqrt{(2 + r_k) \pm \sqrt{(2 + r_k)(r_k - 2r_m)}} \quad (27)$$

It is worth noting that $\omega_R = \omega_0 \sqrt{2 + \kappa}$ is a point of maximum attenuation which corresponds to the discriminant of Eq. (27) being zero in the case where $2r_m = r_k$. The structure of Φ^{NL} ensures that the value of $\Phi^{\text{NL}}(\hat{\omega}_{\pm}) > 1$, which in turn provides information regarding extrema of the imaginary component of the wavenumber $\kappa_1 a$, leading to points where the gradient is zero. The analysis presented here for driven waves can be similarly extended to the different types of phononic materials. For convenience, expressions for $\Phi(\omega)$, ω_R , and $\hat{\omega}$ are given in Table 2.

A comparison between the PC, DP, and NL systems is presented in Fig. 10. The four rows in the figure represent the different dispersion

Table 2 Expressions for Φ for the Phononic Crystal and DP and MP Metamaterials

	$\Phi(\omega)$	ω_R	$\hat{\omega}$
PC	$1 + \frac{r_k \omega^2}{2r_m \omega_0^2} \left(\frac{\omega^2}{\omega_0^2} - (1 + r_m)(1 + 1/r_k) \right)$	—	$\omega_0 \sqrt{\frac{1}{2}(1 + r_m)(1 + 1/r_k)}$
DP	$1 + \frac{r_k \omega^2}{2r_m \omega_0^2} \left(\frac{\omega^2 - \omega_0^2(1 + r_m)}{\omega_0^2 - \omega^2} \right)$	ω_0	No valid solution
MP	$1 + \frac{r_k \omega^2}{2r_m \omega_0^2} \left(\frac{(\omega^2 - \omega_0^2)}{\omega_0^2 - (1 + \frac{\delta}{16} r_k) \omega^2} \right)$	$4\omega_0 \sqrt{\frac{1}{16 + \delta r_k}}$	No valid solution

transitions that are unique to the NL design. The mass and stiffness ratio combinations $[r_m, r_k]$ are $[3, 1]$, $[\frac{3}{2}, 3]$, $[1, 3]$, and $[\frac{1}{3}, 1]$ for Fig. 10A–D, respectively. In each case, the corresponding dispersion diagrams for the PC and DP systems are shown for comparison. In the latter, while the location of the branches (as well as the local resonance ω_R) changes from one row to the next, the overall dispersion shapes are preserved. With a focus on the rightmost column corresponding to the NL metamaterial, and starting with the $2r_m > r_k$ case (Fig. 10A), the dispersion behavior of the NL resembles that of a conventional DP metamaterial and the resonance $\omega_R = \omega_0 \sqrt{2 + \kappa}$ is located inside the band gap. At the turning point (Fig. 10B), $\omega_R = \omega_0 \sqrt{2 + \kappa}$ coincides with the upper limit of the band gap; canceling out the optical branch as a consequence. This also reaffirms the result obtained from Eq. (19) when the group velocity $\frac{\partial \omega}{\partial \kappa} = 0$. By revisiting Eq. (24) with $2r_m = r_k$, the numerator and denominator of the far right term match and the equation reduces to $\Phi^{\text{NL}} = 1 - \frac{\omega^2}{\omega_0^2}$ which explains the lack of an ω_R in such case. Furthermore, a confined band gap ceases

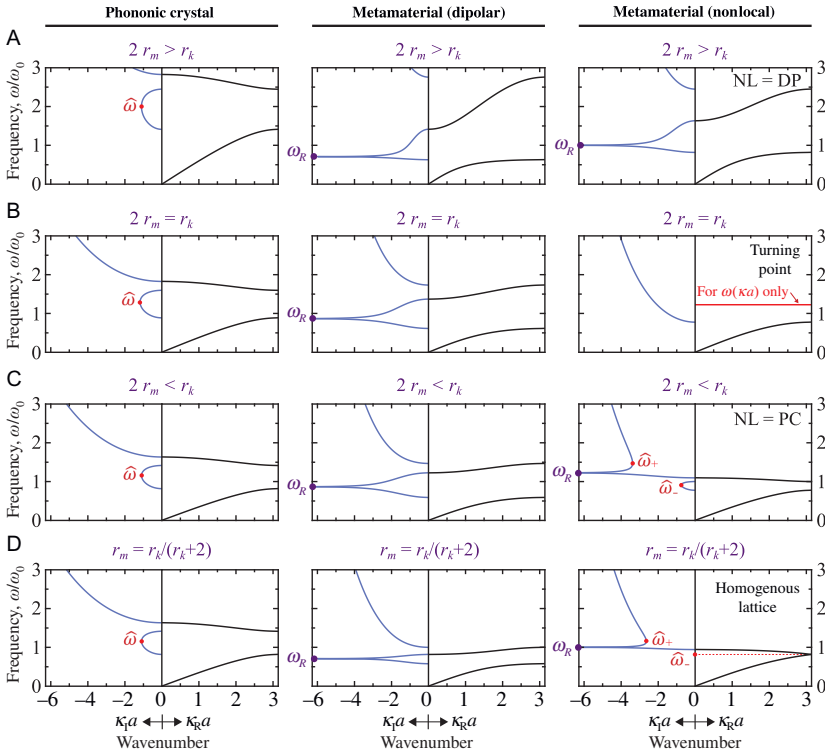
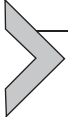


Fig. 10 Dispersion relations for PC (left), DP (middle), and NL (right) for different mass and stiffness ratios: (A) $r_m = 3, r_k = 1$; (B) $r_m = \frac{3}{2}, r_k = 3$; (C) $r_m = 1, r_k = 3$; and (D) $r_m = \frac{1}{3}, r_k = 1$.

to exist. Instead, an unbounded stop band starts immediately at $\omega = \sqrt{2}\omega_0$. For the case when $2r_m < r_k$, $\hat{\omega}_-$ represents the Bragg band-gap maximum attenuation frequency while $\hat{\omega}_+$ reflects an inflection point in the unbounded stop band region, as captured in Fig. 10C. In the final scenario, at $r_m = \frac{r_k}{r_k + 2}$, $\hat{\omega}_-$ coincides with $\omega = \sqrt{2}\omega_0$ when the NL behaves akin to a homogenous monatomic lattice, thus closing the band gap, whereas the inflection point exists at $\hat{\omega}_+ = \omega_0\sqrt{2(1+r_k)}$ as can be seen in Fig. 10D.



4. STATIC EQUIVALENCE AT THE LONG-WAVE SPEED LIMIT

To enable a fair comparison between the dissipation performance of different phononic materials, the systems should be statically equivalent, i.e., exhibit an identical long-wave (sonic) speed c_0 . This condition has been imposed in Section 2.2. In this section, we provide a formal derivation of static equivalence. We start by analytically deriving expressions for c_0 corresponding to the different phononic materials considered, from their respective dispersion relations.

The two solutions for Eq. (14) are given by

$$\omega_{\pm} = \sqrt{\frac{\alpha_1 \pm \sqrt{\alpha_1^2 - 4\alpha_2\alpha_0}}{2\alpha_2}} \quad (28)$$

Of interest here is the solution corresponding to the acoustical branch ω_- , which can be rewritten as

$$\omega_- = \sqrt{\frac{1 - \sqrt{1 - \frac{4\alpha_2\alpha_0}{\alpha_1^2}}}{2\frac{\alpha_2}{\alpha_1}}} \quad (29)$$

To find c_0 , the ratio $\frac{\omega}{\kappa}$ is obtained near $\kappa a = 0$. As can be seen in Table 1, α_0 is a function of the wavenumber κ and its value approaches zero as $\kappa a \rightarrow 0$, resulting in $\frac{4\alpha_2\alpha_0}{\alpha_1^2} \ll 1$. It is important to note that although α_1 may also be a function of κ , depending on the type of phononic material considered, it always has a constant nonzero value when $\alpha = 0$. As a result, the assumption $\frac{4\alpha_2\alpha_0}{\alpha_1^2} \ll 1$ is not affected. Using the binomial approximation $\sqrt{1 - \frac{4\alpha_2\alpha_0}{\alpha_1^2}} \approx 1 - \frac{1}{2}\left(\frac{4\alpha_2\alpha_0}{\alpha_1^2}\right)$, Eq. (29) may be simplified to

$$\omega = \sqrt{\frac{\alpha_0}{\alpha_1}} \quad (30)$$

Further, by utilizing the identity $1 - \cos \kappa a = 2 \sin^2 \frac{\kappa a}{2}$, and for small values of κa (i.e., $\sin^2 \frac{\kappa a}{2} = \left(\frac{\kappa a}{2}\right)^2$), obtaining an expression for c_0 for the PC case is straight forward and takes the form

$$\omega = \kappa a \sqrt{\frac{k_1 k_2}{(m_1 + m_2)(k_1 + k_2)}} \rightarrow c_0^{\text{PC}} = a \omega_0^{\text{PC}} \sqrt{\frac{r_m}{(1 + r_m)(1 + r_k)}} \quad (31)$$

For the remaining types of phononic materials, a Taylor series approximation around $\kappa a = 0$ is needed to further reduce Eq. (30) since both α_0 and α_1 are functions of κa . Now, let us rewrite α_0 and α_1 as $\alpha_0 = \bar{\alpha}_0 \alpha$ and $\alpha_1 = \bar{\alpha}_1 \alpha + \bar{\bar{\alpha}}_1$, respectively, where the corresponding values of the variables $\bar{\alpha}_0$, $\bar{\alpha}_1$, and $\bar{\bar{\alpha}}_1$ can be extracted from Table 1 by matching the coefficients. Substituting $\alpha = 4 \sin^2 \frac{\kappa a}{2}$, Eq. (30) now reads

$$\omega = \sqrt{\frac{4\bar{\alpha}_0 \sin^2 \frac{\kappa a}{2}}{\bar{\bar{\alpha}}_1 + 4\bar{\alpha}_1 \sin^2 \frac{\kappa a}{2}}} = \sqrt{f(\kappa a)} \quad (32)$$

The term under the square root in Eq. (32) can be expanded using a Taylor series around $\kappa a = 0$, which yields

$$f(\kappa a) \simeq f(0) + f'(0)\kappa a + \frac{1}{2}f''(0)(\kappa a)^2 \quad (33)$$

where

$$f'(\kappa a) = \frac{2\bar{\bar{\alpha}}_1 \bar{\alpha}_0 \sin \kappa a}{\left(\bar{\bar{\alpha}}_1 + 4\bar{\alpha}_1 \sin^2 \frac{\kappa a}{2}\right)^2} \quad (34a)$$

$$f''(\kappa a) = 2\bar{\alpha}_0 \bar{\bar{\alpha}}_1 \frac{\bar{\alpha}_1 (2 \cos \kappa a + \cos 2\kappa a - 3) + \bar{\bar{\alpha}}_1 \cos \kappa a}{\left(4\bar{\alpha}_1 \sin^2 \left(\frac{\kappa a}{2}\right) + \bar{\bar{\alpha}}_1\right)^3} \quad (34b)$$

Upon evaluating the first and second derivatives of $f(\kappa a)$ at $\kappa a = 0$, it can be shown that

$$\omega = \kappa a \sqrt{\frac{\bar{\alpha}_0}{\bar{\bar{\alpha}}_1}} \quad (35)$$

and the explicit formulae for the long-wave speed c_0 of DP, MP, and NL metamaterials can be given by

$$c_0^{\text{DP}} = a \omega_0^{\text{DP}} \sqrt{\frac{r_m}{r_k(1 + r_m)}} \quad (36a)$$

$$c_0^{\text{MP}} = a\omega_0^{\text{MP}} \sqrt{\frac{r_m}{r_k}} \quad (36b)$$

$$c_0^{\text{NL}} = a\omega_0^{\text{NL}} \sqrt{\frac{(2/r_k + 1)}{2(1 + 1/r_m)}} \quad (36c)$$

The above equations may be rearranged with the long-wave speed c_0 as an input to obtain the corresponding ω_0 , resulting in

$$\omega_0^{\text{PC}} = \frac{c_0^{\text{PC}}}{a} \sqrt{(1 + r_k)(1 + 1/r_m)} \quad (37a)$$

$$\omega_0^{\text{DP}} = \frac{c_0^{\text{DP}}}{a} \sqrt{r_k(1 + 1/r_m)} \quad (37b)$$

$$\omega_0^{\text{MP}} = \frac{c_0^{\text{MP}}}{a} \sqrt{\frac{r_k}{r_m}} \quad (37c)$$

$$\omega_0^{\text{NL}} = \frac{c_0^{\text{NL}}}{a} \sqrt{\frac{2(1 + 1/r_m)}{(2/r_k + 1)}} \quad (37d)$$

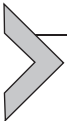
By setting c_0 of the PC as the benchmark for comparison, and maintaining identical c_0 values for the rest of the designs, alternative expressions for the frequency ω_0 as a function of ω_0^{PC} for the metamaterial counterparts can be derived as

$$\omega_0^{\text{DP}} = \omega_0^{\text{PC}} \sqrt{\frac{r_k}{1 + r_k}} \quad (38a)$$

$$\omega_0^{\text{MP}} = \omega_0^{\text{PC}} \sqrt{\frac{r_k}{(1 + r_m)(1 + r_k)}} \quad (38b)$$

$$\omega_0^{\text{NL}} = \omega_0^{\text{PC}} \sqrt{\frac{2r_k}{(1 + r_k)(2 + r_k)}} \quad (38c)$$

For instance, if we look specifically at $c_0 = 40$ (see Fig. 6), using Eq. (31) and the parameters $r_m = 3$, $r_k = 1$, and $a = 1$, results in $\omega_0^{\text{PC}} = 65.32$. Finally, by making use of Eqs. (38a)–(38c), the equivalent frequencies ω_0 for each of the DP, MP, and NL are $\omega_0^{\text{DP}} = 46.19$, $\omega_0^{\text{MP}} = 23.09$, and $\omega_0^{\text{NL}} = 37.71$, respectively.



5. METADAMPING IN NONLOCAL METAMATERIALS

In Section 3, the intriguing features associated with the dispersion characteristics of undamped NL metamaterials were thoroughly discussed. Now we examine and highlight the dissipative performance of the NL

metamaterial in the presence of damping elements, and draw comparisons with the PC and DP chains (a comparison with the MP system is omitted for brevity). In the presence of the dashpots c_1 and c_2 , the mass, damping and stiffness matrices are given by

$$\mathbf{M} = m_2 \begin{bmatrix} 1/r_m & 0 & 0 \\ 0 & 1 & 0 \\ 0 & 0 & 0 \end{bmatrix} \quad (39a)$$

$$\mathbf{C} = c_2 \begin{bmatrix} (1/r_c + 1/2) & -1/2 & -1/r_c \\ -1/2 & 1 & -1/2 \\ -1/r_c & -1/2 & (1/r_c + 1/2) \end{bmatrix} \quad (39b)$$

$$\mathbf{K} = k_2 \begin{bmatrix} (1/r_k + 1) & -1 & -1/r_k \\ -1 & 2 & -1 \\ -1/r_k & -1 & (1/r_k + 1) \end{bmatrix} \quad (39c)$$

The dispersion characteristic of the dissipative NL metamaterial is obtained by invoking the Bloch boundary condition via the transformation matrix \mathbf{T} as introduced earlier, and using the state-space formulation to obtain the complex frequencies λ . Similar to the example presented in Fig. 6, all the systems undergoing comparisons are statically equivalent with a long-wave speed of $c_0 = 40$ and identical stiffness and mass ratios. Recall that the damping intensity ratio is $\beta/\omega_0^{\text{PC}} = 0.1$ from which the damping coefficients are computed as $c_2 = \beta m_2$ and $c_1 = c_2/r_c$. Since the NL metamaterial comprises an extra c_2 damper in each unit cell when compared to the PC and DP configurations, the value of c_2 is halved to maintain a fair comparison, which is reflected in the \mathbf{C} matrix in Eq. (39b). While keeping the same damping coefficients, we investigate the metadamping effects with a second set of parameters leaving r_m unchanged and setting $r_k = 3$. The adjusted ω_0 values for the second set of parameters are $\omega_0^{\text{PC}} = 92.38$, $\omega_0^{\text{DP}} = 80$, and $\omega_0^{\text{NL}} = 50.6$.

Figs. 11 and 12 depict the dispersion curves and the damping ratios across the optical and acoustical bands for the first and second set of parameters, respectively. It is evident from both figures that the overall drop of the optical branch in response to increased damping is larger in the NL than it is in the DP system. Furthermore, the change in the stiffness ratio generates a larger increase in the damping ratio in the NL than in the DP. In both cases, the damping ratios of the NL is either slightly or considerably higher than that of the DP metamaterial, while both metamaterial designs exhibit larger

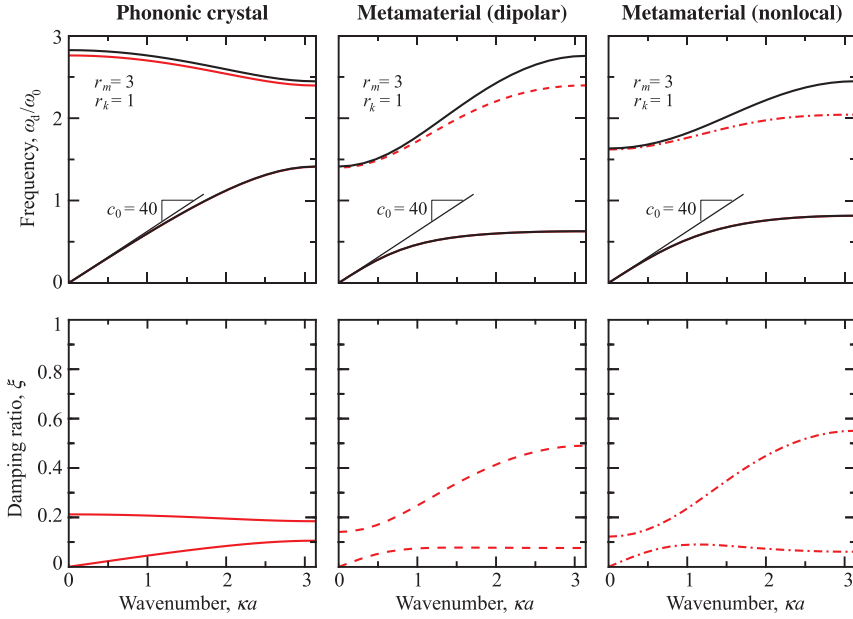


Fig. 11 Dispersion curves and corresponding damping ratios for the damped PC, DP, and NL systems with $r_m = 3$, $r_k = 1$, and $c_0 = 40$.

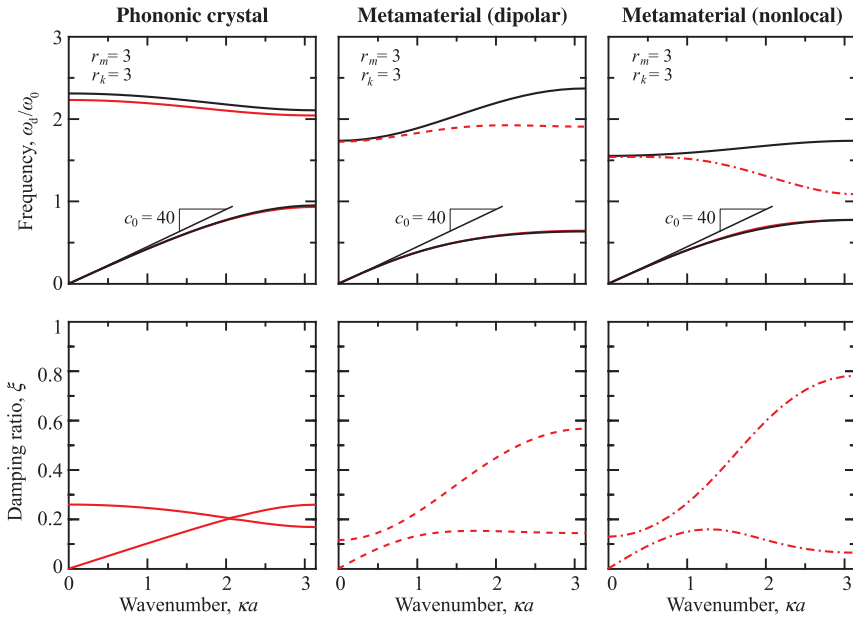


Fig. 12 Dispersion curves and corresponding damping ratios for the damped PC, DP, and NL systems with $r_m = 3$, $r_k = 3$, and $c_0 = 40$.

damping ratios than the PC. Following the earlier analysis, the averaged damping ratio ξ_{avg} is computed from the integration of $(\xi_1 + \xi_2)$ over the wavenumber κa ranging from 0 to π (as can be seen in Eq. (13)). The sonic speed c_0 is swept over a range of values while keeping the same mass and stiffness ratios as well as the damping amount, by adjusting the value of ω_0 for each system, respectively. The outcome of this process is graphically presented in Figs. 13 and 14 which correspond to the cases discussed in Figs. 11 and 12, respectively. It is evident that the NL outperforms the

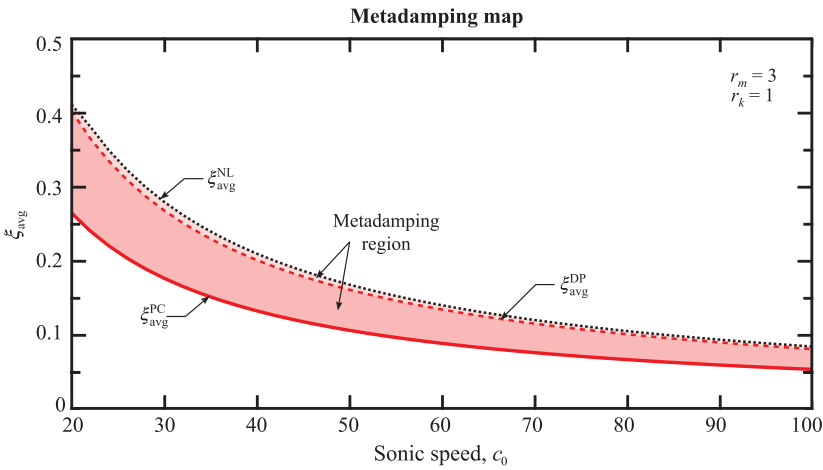


Fig. 13 Metadamping regions in the NL and DP metamaterials (compared to the PC as a datum) for $r_m = 3$, $r_k = 1$.

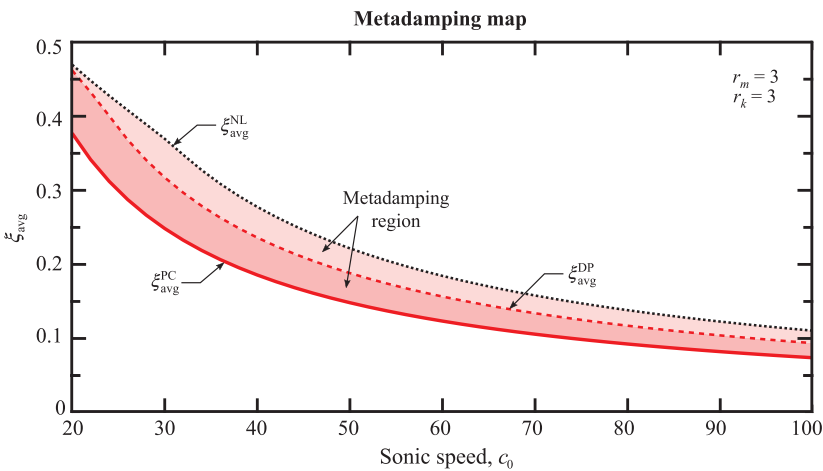


Fig. 14 Metadamping regions in the NL and DP metamaterials (compared to the PC as a datum) for $r_m = 3$, $r_k = 3$.

PC and the DP systems in terms of total metadamping in both cases. The amplified metadamping emergence in the NL is particularly observed with the second set of parameters, validating the damping ratio diagrams presented in Fig. 12.

6. PARAMETRIC STUDY OF METADAMPING

As revealed in the previous section, the change in the stiffness ratio r_k enhanced the metadamping emergence in the NL metamaterial for a prescribed set of damping coefficients and ratio r_c . As such, it is imperative to investigate this phenomenon further across a broader spectrum of properties and material variations, while maintaining to the extent possible reasonable constraints that render such comparisons just. We start by examining the effect of increasing the damping amount (i.e., varying the values of c_1 and c_2) as well as the choice of the ratio r_c (reflecting the damping distribution across the two materials). Fig. 15 combines the effect of the increasing the damping intensity ratio β/ω_0 with different choices of $c_{1,2}$ for the three phononic materials under consideration: the PC, DP, and the NL. Other parameters used in the comparison are identical to those selected in Fig. 12: $r_k = r_m = 3$ and $c_0 = 40$. In each subplot of Fig. 15, three separate cases are considered: (1) $c_2 = 0$ (i.e., $r_c = 0$) and $c_1 = \beta m_2$, (2) $c_1 = 0$ (i.e., $r_c = \infty$) and $c_2 = \beta m_2$, and (3) $r_c = 1$ (with $c_1 = c_2 = \beta m_2/2$). It is noted that in the last case, the damping coefficients are reduced to half their previous values to keep the total damping amount constant across the board. It is first observed that the average damping ratio ξ_{avg} increases linearly with an increase in the damping intensity ratio, irrespective of the phononic material type, for all combinations of c_1 and c_2 . However, it can be seen that the damping distribution within the same phononic material

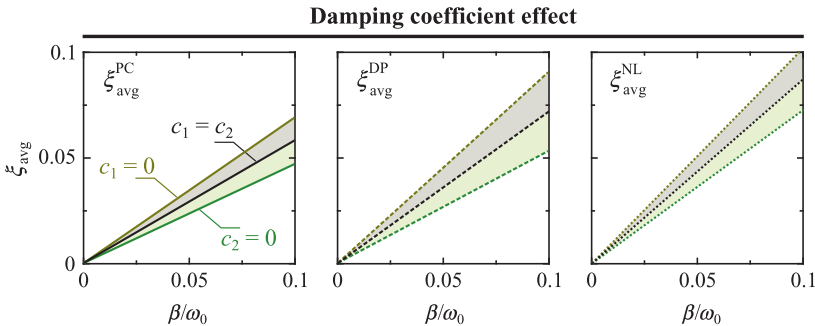


Fig. 15 Metadamping variation with the damping intensity ratio β/ω_0 between the PC, DP, and NL systems for $r_k = r_m = 3$ and $c_0 = 40$.

plays an influential role in the emergent metadamping. Between the two extreme cases corresponding to $r_c = 0$ (i.e., $c_2 = 0$) and $r_c = \infty$ (i.e., $c_1 = 0$), the latter exhibits larger metadamping for the same amount of total damping injected in the system. The metadamping in the case $c_1 = c_2$ lies halfway between the two extreme damping distributions.

With both damping coefficients c_1 and c_2 kept constant, the implications of changing other material properties in the phononic design are also investigated. Fig. 16 shows the variation of metadamping with increasing damping intensities for the two stiffness ratios $r_k = 1$ and $r_k = 3$ examined earlier. As an initial takeaway, it can be seen that the metadamping corresponding to $r_k = 3$ (and reflected by the metadamping metric ξ_{avg}) quantitatively exceeds that of the $r_k = 1$ design for all three systems considered. The previous is also in line with Figs. 11 and 12. In addition, the linear relationship between the damping intensity and the metric ξ_{avg} remains intact. The relative enhancement of the metadamping across the different phononic materials given a prescribed set of parameters may be computed using the metric \mathbf{Z} , illustrated in the rightmost panel of Fig. 16. For example,

$$\mathbf{Z}_{\text{DP}}^{\text{NL}} = \xi_{\text{avg}}^{\text{NL}} - \xi_{\text{avg}}^{\text{DP}} \quad (40)$$

defines the relative enhancement (or deterioration) of the emergent metadamping in the NL metamaterial as compared to a corresponding DP metamaterial. Using the newly defined \mathbf{Z} as a metric to assess relative metadamping improvements, or lack thereof, design charts that comprise variations in material properties such as mass, stiffness, and damping ratios, and the interplay between them may be constructed. Investigating the damping distributions across the different constituents of a phononic material allows us to enhance the metadamping outcome. To do so, the stiffness ratio is swept between the values of 0.01–100 and is varied against the ratio r_c . Contours of the relative metadamping metric \mathbf{Z} as a function of both r_k

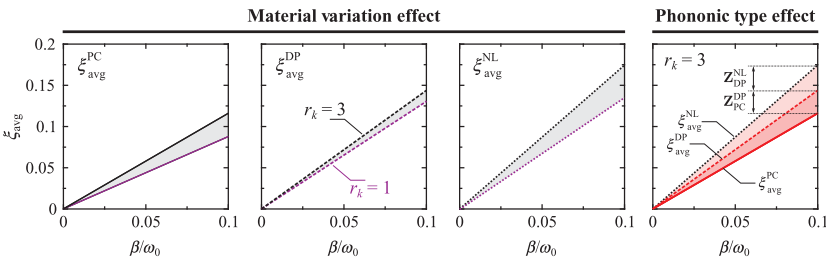


Fig. 16 Effect of material properties (*left*) and phononic material type (*right*) on metadamping for $r_c = 1$.

and r_c are then generated. For a given (constant) amount of prescribed damping η , the two damping coefficients c_1 and c_2 may be computed as

$$c_1 = \frac{\eta}{(1 + r_c)} \quad (41a)$$

$$c_2 = \frac{\eta}{(1 + 1/r_c)} \quad (41b)$$

For $\eta = 15$ and maintaining $\omega_0^{\text{PC}} = 100$ throughout, Fig. 17 displays the relative metadamping differences $\mathbf{Z}_{\text{PC}}^{\text{DP}}$, $\mathbf{Z}_{\text{PC}}^{\text{NL}}$, and $\mathbf{Z}_{\text{DP}}^{\text{NL}}$, as well as the corresponding sonic speed as computed from Eq. (31). Recall that the adjusted ω_0^{DP} and ω_0^{NL} can be obtained from Eqs. (38a) and (38c), respectively. These charts show that the metadamping effectiveness is largely affected by the distribution of damping among the different materials of the phononic material, in addition to the material properties (represented by r_k). For instance, in the case of $\mathbf{Z}_{\text{PC}}^{\text{NL}}$, the metadamping enhancement is seen to increase as we move further away from $r_k = 1$. Furthermore, a large metadamping effect accompanies large values of r_k almost consistently irrespective of r_c . For small r_k , however, the metadamping effect only becomes as significant with larger r_c values. Additionally, the maps also show unfavorable regions (shaded area in Fig. 17) such as in the case of $\mathbf{Z}_{\text{DP}}^{\text{NL}}$, where the metadamping in the conventional DP metamaterial outperforms its counterpart in the NL system.

In addition to confirming the metadamping emergence in resonant metamaterials (e.g., the DP and NL systems) when compared to a common benchmark in the form of a PC system, Fig. 17 also gives a physical insight into how the metadamping in the NL system compares to that of a conventional DP metamaterial. The ability of DP metamaterials to exhibit metadamping gradually vanishes as the stiffness of the local resonator becomes very high to the extent that constrains the internal vibrations and consequently renders the internal resonance dynamics ineffective. This can be noticeably observed in the leftmost plot of Fig. 17 where $\mathbf{Z}_{\text{PC}}^{\text{DP}}$ goes to zero at high values of the stiffness

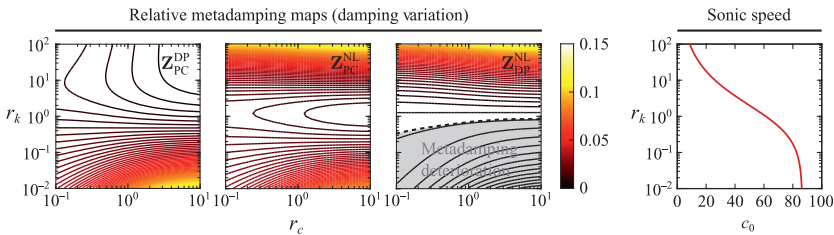


Fig. 17 Contours of the relative metadamping differences $\mathbf{Z}_{\text{PC}}^{\text{DP}}$, $\mathbf{Z}_{\text{PC}}^{\text{NL}}$, and $\mathbf{Z}_{\text{DP}}^{\text{NL}}$ with variations in r_k and r_c . The corresponding sonic speed is provided for reference.

ratio r_k , signaling that the DP and PC systems basically become identical from the standpoint of metadamping. NL metamaterials alleviate this situation by providing a unit cell configuration where the resonator is not completely isolated from the periodic chain and thus mitigates the effect of a high resonator stiffness, all while still maintaining some attributes of an elastic metamaterial as evident by the dispersion diagrams in Fig. 10. As a result, the metadamping in the NL system outperforms that in the DP system and \mathbf{Z}_{PC}^{NL} exhibits values greater than zero at higher values of r_k . Once the resonator stiffness is reduced again, the DP metamaterial recovers its metadamping advantage over the NL design, as can be seen in the behavior of \mathbf{Z}_{DP}^{NL} . The latter corresponds to the region marked ‘‘Deterioration’’ in the rightmost plot of Figure 17.

Analogous to the variations in r_c , the analysis may be extended to depict changes in the metadamping performance with mass and stiffness ratios that span a larger design space. This is shown in Fig. 18 for constant damping coefficients. The damping ratio ξ corresponding to the optical branch at $\kappa a = \pi$ is provided in Fig. 19 for reference. Fig. 19 is used as a precautionary measure to ensure that none of the results displayed in Fig. 18 pertain to an overdamped system (i.e., $\xi > 1$) with a nonoscillatory response which is not of interest in the current analysis. It is also worth noting that some parameter

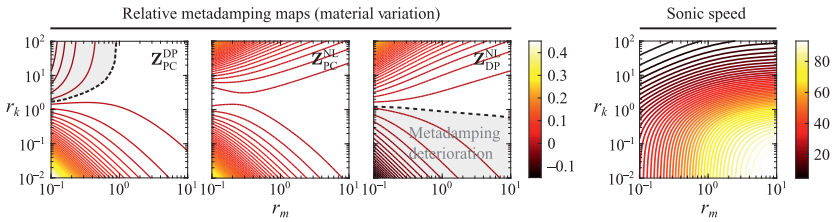


Fig. 18 Contours of the relative metadamping differences \mathbf{Z}_{PC}^{DP} , \mathbf{Z}_{PC}^{NL} and \mathbf{Z}_{DP}^{NL} for identical damping coefficients ($c_1 = c_2 = 2$) and variations in r_k and r_m . ω_0^{PC} is kept at 100 for all the considered cases. The corresponding sonic speed is provided for reference.

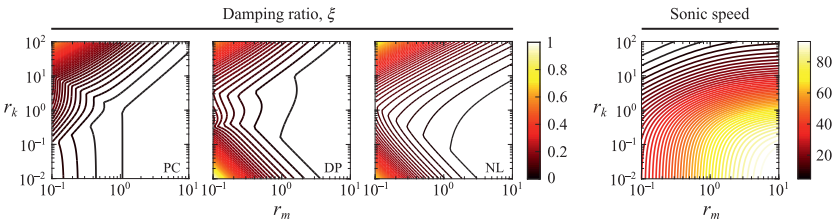
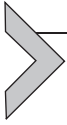


Fig. 19 Damping ratio ξ of the optical dispersion branch at $\kappa a = \pi$ corresponding to the relative metadamping maps provided in Fig. 18.

choices result in negative values for both \mathbf{Z}_{PC}^{DP} and \mathbf{Z}_{DP}^{NL} ; an indication of a performance deterioration from a metadamping standpoint. On the contrary, \mathbf{Z}_{PC}^{NL} show improvement for the entire design space considered. These charts constitute a comprehensive framework and serve as design guidelines for the type of phononic material, the material properties, as well as the distribution of damping within the same phononic material to yield optimal metadamping levels.



7. EFFECT OF CORE DAMPING MODEL

In the previous sections, the concept of metadamping was presented in the context of viscous damping, i.e., simple dashpot elements. However, accurate and realistic prediction of material damping typically requires different, and often more complex, models. A natural extension of this work is to investigate to what degree the intriguing metadamping attributes established earlier apply to slightly more involved damping models. Means of accounting for damping in structural mechanics include the use of complex elastic moduli (Castanier & Pierre, 1993; Sprik & Wegdam, 1998; Zhang, Liu, Mei, & Liu, 2003) or inertial terms (Langley, 1994b), as well as stand-alone parameters which are functions of velocity (Hussein, 2009b; Hussein & Frazier, 2010). The choice of the damping model usually depends on the application and is critical to minimize discrepancies at the experimental stages (Adhikari & Phani, 2009; Phani & Woodhouse, 2007, 2009). Here, we extend the previous discussion to the viscoelastic regime and specifically the Maxwell element (see Fig. 20) to model the viscoelasticity (Frazier & Hussein, 2015). The mathematical formulation developed in Section 1.2 is slightly modified to accommodate for the differences in the damping mechanism as will be illustrated in the forthcoming section.

7.1 Viscoelasticity: Background and Modeling

Viscoelasticity is a property of a material that simultaneously exhibits viscous and elastic behaviors. As a result, a coupling of the damping and the stiffness properties within the material provides the damping element with

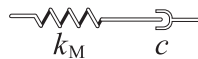


Fig. 20 A schematic of the Maxwell element where the stiffness (conservative) and damping (nonconservative) elements are connected in series.

an energy storage capability. Unlike viscous damping, which is primarily observed in viscous fluids (Woodhouse, 1998), viscoelastic damping is a hereditary model which takes into consideration the past and present history of the dynamical motion whereby dissipation is attributed to a phase shift between the displacement and stress fields (Bert, 1973; Nouh, Aldraihem, & Baz, 2015). Owing to the nature of the viscoelasticity, the mathematical treatment of the viscoelastic model includes internal states $\hat{\mathbf{p}}_j$ which are computed using a convolution integral over an exponentially decaying kernel function $G(t) = \mu_{1,j}e^{-\mu_{2,j}t}$ (where $\mu_{1,j}$ and $\mu_{2,j}$ are the relaxation pairs) capturing the entire motion up to and including the current state (Wagner & Adhikari, 2003). For an equal pair of relaxation parameters, i.e., $\mu_j = \mu_{1,j} = \mu_{2,j}$, the j -th internal state is given by the following convolution integral (Frazier & Hussein, 2015)

$$\hat{\mathbf{p}}_j = \int_0^t \mu_j e^{-\mu_j(t-\tau)} \dot{\mathbf{u}}(\tau) d\tau \quad (42)$$

and, hence, Eq. (5) is rewritten as

$$\hat{\mathbf{M}}\ddot{\mathbf{u}} + \sum_{j=1}^{\ell} \hat{\mathbf{C}}_j \hat{\mathbf{p}}_j + \hat{\mathbf{K}}\hat{\mathbf{u}} = \mathbf{0} \quad (43)$$

where ℓ is the total number of internal states. To attain the time derivative of $\hat{\mathbf{p}}_j$, the Leibniz integral rule is applied to Eq. (42) resulting in

$$\dot{\hat{\mathbf{p}}}_j = - \int_0^t \mu_j^2 e^{-\mu_j(t-\tau)} \dot{\mathbf{u}}(\tau) d\tau + \mu_j \dot{\mathbf{u}} = \mu_j \left[\dot{\mathbf{u}} - \hat{\mathbf{p}}_j \right] \quad (44)$$

following which, substituting back into Eq. (43) gives

$$\hat{\mathbf{M}}\ddot{\mathbf{u}} + \sum_{j=1}^{\ell} \hat{\mathbf{C}}_j \left[\dot{\mathbf{u}} - \frac{1}{\mu_j} \dot{\hat{\mathbf{p}}}_j \right] + \hat{\mathbf{K}}\hat{\mathbf{u}} = \mathbf{0} \quad (45)$$

Eq. (45) in its current form cannot be readily used in the state-space representation presented earlier since it would result in nonsquare matrices. Premultiplying Eq. (44) by $\frac{1}{\mu_j} \hat{\mathbf{C}}_j$ and rearranging yields

$$\frac{1}{\mu_j} \hat{\mathbf{C}}_j \dot{\hat{\mathbf{p}}}_j - \frac{1}{\mu_j^2} \hat{\mathbf{C}}_j \dot{\hat{\mathbf{p}}}_j - \frac{1}{\mu_j} \hat{\mathbf{C}}_j \dot{\mathbf{u}} = \mathbf{0} \quad (46)$$

Plugging Eq. (46) into Eq. (45), the state-space matrices $\hat{\mathbf{A}}$ and $\hat{\mathbf{B}}$ can now be cast as

$$\hat{\mathbf{A}} = \begin{bmatrix} \mathbf{0} & \hat{\mathbf{M}} & \mathbf{0} & \mathbf{0} & \dots & \mathbf{0} \\ \hat{\mathbf{M}} & \sum_{j=1}^{\ell} \hat{\mathbf{C}}_j & -\frac{1}{\mu_1} \hat{\mathbf{C}}_1 & -\frac{1}{\mu_2} \hat{\mathbf{C}}_2 & \dots & -\frac{1}{\mu_{\ell}} \hat{\mathbf{C}}_{\ell} \\ \mathbf{0} & -\frac{1}{\mu_1} \hat{\mathbf{C}}_1 & \frac{1}{\mu_1^2} \hat{\mathbf{C}}_1 & \mathbf{0} & \dots & \mathbf{0} \\ \mathbf{0} & -\frac{1}{\mu_2} \hat{\mathbf{C}}_2 & \mathbf{0} & \frac{1}{\mu_2^2} \hat{\mathbf{C}}_2 & \dots & \mathbf{0} \\ \vdots & \vdots & \vdots & \vdots & \ddots & \vdots \\ \mathbf{0} & -\frac{1}{\mu_{\ell}} \hat{\mathbf{C}}_{\ell} & \mathbf{0} & \mathbf{0} & \dots & \frac{1}{\mu_{\ell}^2} \hat{\mathbf{C}}_{\ell} \end{bmatrix} \quad (47a)$$

$$\hat{\mathbf{B}} = \text{diag} \left[-\hat{\mathbf{M}} \quad \hat{\mathbf{K}} \quad \frac{1}{\mu_1} \hat{\mathbf{C}}_1 \quad \frac{1}{\mu_2} \hat{\mathbf{C}}_2 \quad \dots \quad \frac{1}{\mu_{\ell}} \hat{\mathbf{C}}_{\ell} \right] \quad (47b)$$

where $\hat{\mathbf{y}}^T = [\dot{\hat{\mathbf{u}}} \quad \hat{\mathbf{u}} \quad \hat{\mathbf{p}}_1 \quad \hat{\mathbf{p}}_2 \quad \dots \quad \hat{\mathbf{p}}_{\ell}]$ is the new state vector. While multiple internal states $\hat{\mathbf{p}}_j$ more accurately describe the viscoelastic working mechanism, the focus of the present analysis is to highlight the differences between the viscoelastic and viscous damping and, therefore, a single kernel function (i.e., $\ell = 1$) is sufficient to describe the viscoelastic phenomenon; Eq. (8) now reads

$$\left(\lambda \begin{bmatrix} \mathbf{0} & \hat{\mathbf{M}} & \mathbf{0} \\ \hat{\mathbf{M}} & \hat{\mathbf{C}} & -\frac{1}{\mu} \hat{\mathbf{C}} \\ \mathbf{0} & -\frac{1}{\mu} \hat{\mathbf{C}} & \frac{1}{\mu^2} \hat{\mathbf{C}} \end{bmatrix} + \begin{bmatrix} -\hat{\mathbf{M}} & \mathbf{0} & \mathbf{0} \\ \mathbf{0} & \hat{\mathbf{K}} & \mathbf{0} \\ \mathbf{0} & \mathbf{0} & \frac{1}{\mu} \hat{\mathbf{C}} \end{bmatrix} \right) \hat{\mathbf{y}} = \mathbf{0}. \quad (48)$$

Upon computing the eigenvalues of Eq. (48), the real nonoscillatory modes corresponding to the internal states can be found. The remaining modes are complex pairs which dictate wave propagation in the dissipative structure, as long as that the prescribed damping intensity β does not render the system overdamped (i.e., $\xi > 1$). It is worth noting that in the extreme cases where $\mu \rightarrow 0$ and $\mu \rightarrow \infty$, Eq. (48) recovers the undamped and viscously damped state matrices, respectively. With $\mu \rightarrow 0$, and since $k_M \propto \mu$, the spring in Fig. 20 softens and eventually disengages. On the other hand, for $\mu \rightarrow \infty$, the spring stiffens and effectively becomes a rigid connection. As a consequence, most of the energy is dissipated in the damping element c .

7.2 Metadamping in Viscoelastic Phononic Materials

7.2.1 Viscous-to-Viscoelastic Transition

In this section, we revisit the example in Fig. 11 and apply the viscoelastic model for the same parameters to capture the transition between viscous to viscoelastic damping. If the relaxation parameter $\mu = 300$ is used to generate the viscoelastic counterpart of Fig. 11, the result will be as depicted in Fig. 21 where the undamped and viscously damped cases are also plotted for reference. In all the shown cases, the optical branches as expected demonstrate higher tendency to deviate from the undamped case given the higher frequency range. The acoustical branches remain nearly unchanged. The introduction of viscoelastic damping tends to increase the damped frequency since some of the energy in the Maxwell element is conserved (unlike the viscous model which effectively decreases the damped frequency). This increase in the damped frequency of the optical branch widens the band gap, an effect that is more pronounced in the case of the PC. Since part of the energy is stored in the viscoelastic model, we expect the damping ratios of the viscoelastic systems to be lower than those of the viscous ones across all the phononic materials considered. This can be noticeably observed in the lower panel of Fig. 21.

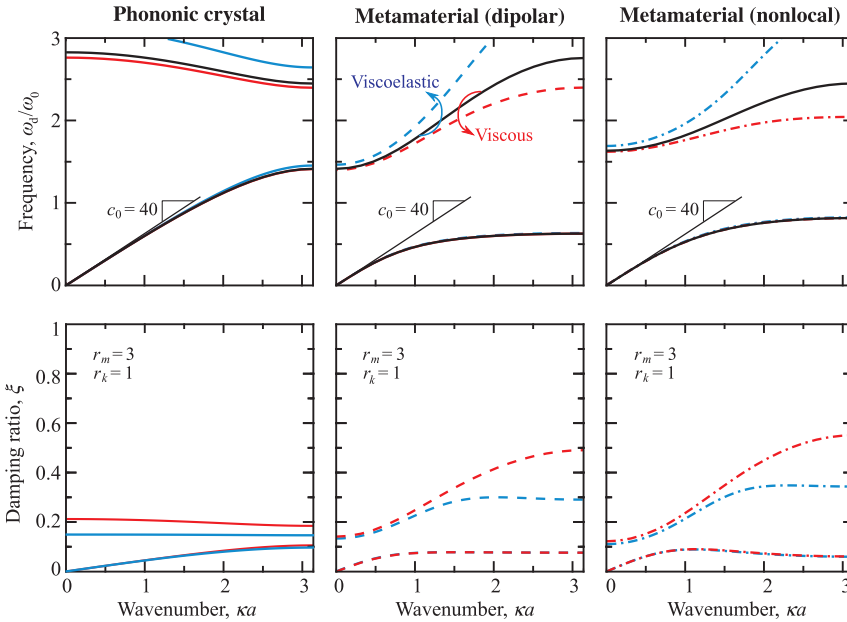


Fig. 21 Comparison of the dispersion curves and corresponding damping ratios for the PC, DP, and NL systems under viscous and viscoelastic models.

7.2.2 Band-Gap Limits

The evolution of the band-gap limits as well as the band-gap width $\Delta\omega_d$ for all the different viscoelastic phononic materials is shown in Fig. 22 by the solid curves. The dashed lines denote the viscous and undamped models and are shown for comparison. The narrowest band gaps take place when the phononic material has fully developed into the viscous damping regime. During the transition, the band-gap width for the PC peaks in the vicinity of $\mu = 200$, while for the NL and DP metamaterials, the largest band-gap width occurs around $\mu = 120$. These peaks happen as the energy storage capability in the Maxwell element reaches its maximum value thus overshadowing the amount of dissipated energy (Frazier & Hussein, 2015).

Despite the increase in the band-gap width, we anticipate the metadamping emergence in the viscoelastic phononic materials to deteriorate. This can also be inferred from the damping ratio ξ comparisons displayed in Fig. 21. Following a similar procedure to that used to generate Fig. 13, and using $\mu = 300$, the

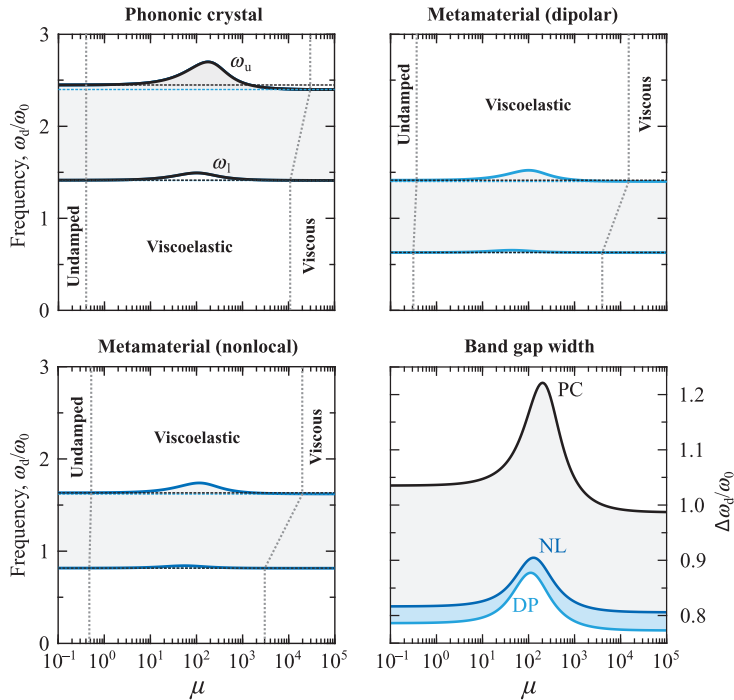


Fig. 22 Evolution of band-gap limits for the PC, DP, and NL systems as a function of the relaxation parameter μ . The figure illustrates the transition lines between the undamped, viscoelastic and viscous regimes. *Black and blue dashed lines* represent the band-gap limits of the undamped and the viscous models, respectively.

sonic speed c_0 is swept across a range of values and the corresponding metadamping ξ_{avg} for the viscoelastic phononic materials is evaluated. The relative metadamping performances of the PC, DP, and NL systems are shown in Fig. 23A. Further, a comparison of the emergent metadamping between the viscoelastic and the viscous systems is presented in Fig. 23B–D. Examining these patterns, it can be seen that the sensitivity of the metadamping to the damping model decreases at lower sonic speeds where, for the given relaxation parameter, the viscoelastic model becomes nearly viscous.

Finally, the evolution of metadamping with the change in the damping regimes (i.e., the degree of the hereditary model) is computed as a function of μ for the different phononic materials in Fig. 24. The metadamping increases as μ increases for all the phononic materials up until a certain degree of saturation as the systems completely transition into the viscous regime. In contrast to the PC, the DP and NL metamaterials exhibit a ξ_{avg} peak in the neighborhood of the transition line between the viscous and viscoelastic models. Such unique traits which manifest themselves from the integration

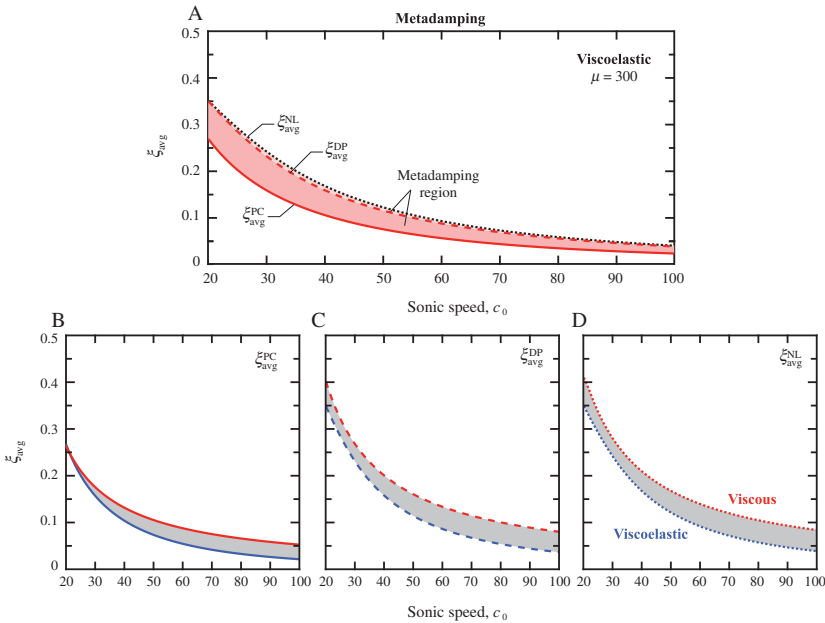


Fig. 23 (A) Metadamping emergence in NL and DP metamaterials with viscoelastic damping ($\mu = 300$). (B)–(D) Quantitative comparisons between the viscoelastic and the viscous metadamping curves for the PC, DP, and NL systems, respectively.

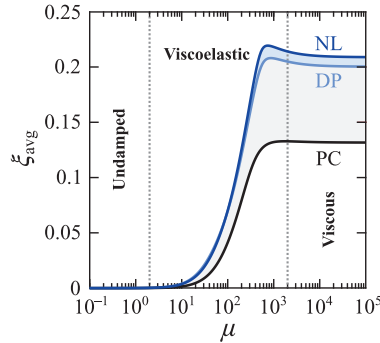
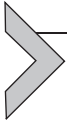


Fig. 24 Metadamping in the PC, DP, and NL systems as a function of the relaxation parameters μ . Transition between the different regimes is illustrated by the *dotted lines*.

of the material damping with the different phononic materials open up new avenues in material designs for optimal wave absorption as well as broadband attenuation performances.



8. EXPERIMENTAL VALIDATION OF METADAMPING

In the previous sections, the concept of metadamping has been presented and analyzed in the context of lumped mass–spring–dashpot systems. Although these simple models provide a clear demonstration of the concept, with the added advantage of enabling closed-form analytical solutions, a more elaborate model is needed to examine suitability for real-world applications and to enable proper experimental validation.

In this section, we examine metadamping in an experimental configuration, and a corresponding numerical model, in the form of an extended all-aluminum beam with pillars periodically standing out—along the axial axis—from one of the beam’s surfaces (see Figs. 25 and 26) (Bacquet & Hussein, 2018). The pillars serve the role of the resonating substructures; they are shaped by milling to ensure seamless connectivity. Our choice of a medium with one-dimensional periodicity is only for ease of exposition as the underlying dynamical behavior we are interested in takes place for any dimension and is in fact independent of periodicity (Achaoui, Laude, Benchabane, & Khelif, 2013). This investigation consists of two parts. In the first part, we use experiments and corresponding finite-element simulations applied to a four-celled finite-sized version of the pillared

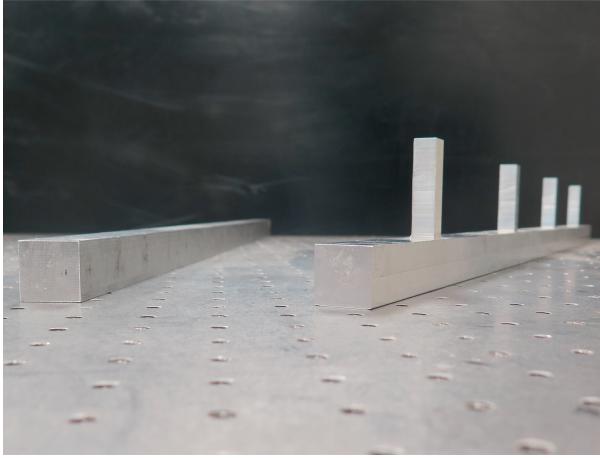


Fig. 25 Photograph of the two experimental structures: the unpillared beam (*left*) and the pillared beam (*right*).

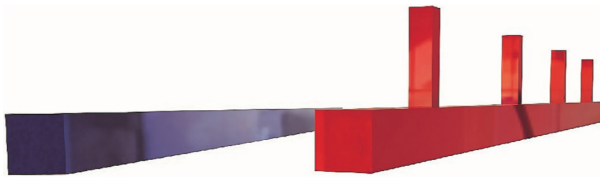


Fig. 26 Numerical models of the two experimental structures: the unpillared beam (*left*) and the pillared beam (*right*).

beam to provide evidence of metadamping. In the second part, we provide a correlation of the observed behavior with the dispersion and damping ratio diagrams for the unit cell from which the pillared beam structure is formed.

8.1 Pillared Beam: One-Dimensional Metamaterial

We consider the following two test structures composed entirely from aluminum: a regular beam (unpillared) and a metamaterial beam (pillared). The unpillared beam's dimensions are $32 \times 1 \times 1$ inches. The pillared beam has the same underlying beam base, but is augmented with four squares pillars ($0.5 \times 0.5 \times 2$ inches) which are periodically arranged along the axial direction. These pillars act as the local resonators; there is one pillar per unit cell. Fig. 25 shows a photograph of both structures in the laboratory, and Fig. 26 depicts the corresponding numerical models. Throughout this section, the

color blue will represent the unpillared beam and the color red will represent the pillared beam.

8.1.1 Experimental Setup

Each of the beam structures is suspended using nylon cords in order to simulate free-free boundary conditions. An accelerometer (PCB WJ35C65) is attached at the center point of the cross section on one of the ends of the beam. Impulsive excitations are applied with an impact hammer (PCB 086C02) at a point located at the center of the opposite cross section, such that only the longitudinal modes are excited and measured. The measurements are collected with a NI-DAQ 9234 data acquisition system (the frequency rate is set to 25.6 kHz and the sample time is 5 s). Five time series are recorded and averaged for each beam. The inertance spectrum is obtained by postprocessing the time data using a commercial software package (MATLAB[®], The MathWorks Inc., Natick, MA, United States). Fig. 27A shows the experimental frequency response functions (FRF) obtained by this process. The reader is referred to the review article Hussein et al. (2014) and the recent article Al Ba'ba'a, Attarzadeh, and Nouh (2017) for examples of other experimental setups for phononic systems.

8.1.2 Numerical Model

The two beam structures are numerically modeled with the following prescribed material properties: density of $\rho = 2700 \text{ kg/m}^3$, Young's modulus of $E = 68.9 \text{ GPa}$, and Poisson's ratio of $\nu = 0.33$. Using the finite-element (FE) method for spatial discretization, we adopt a viscoelastic damping model of the form (Frazier & Hussein, 2015; Hussein & Frazier, 2013a; Wagner & Adhikari, 2003)

$$\mathbf{M}\ddot{\mathbf{u}}(t) + \int_{k=1}^t \mu e^{-\mu(t-\tau)} \mathbf{C}\dot{\mathbf{u}}(\tau) d\tau + \mathbf{K}\mathbf{u}(t) = \mathbf{f}(t), \quad (49)$$

where, for simplicity, the FE damping matrix \mathbf{C} is assumed to be proportional to the FE mass \mathbf{M} and stiffness \mathbf{K} matrices, such that $\mathbf{C} = p\mathbf{M} + q\mathbf{K}$. The FE model consists of three-dimensional 8-node brick FE (total number of elements in the unit cell are 4096 for the unpillared beam and 4352 for the pillared beam). The parameters p and q , as well as a relaxation parameter μ , are determined by a unique experimental material-structure curve-fitting procedure described in Bacquet and Hussein (2018), which has provided us with the values $p = 22$, $q = 2.2 \times 10^{-7}$, and $\mu = 10^4$. Information on the FE implementation is available in Hussein (2009 a); and information on the viscoelastic

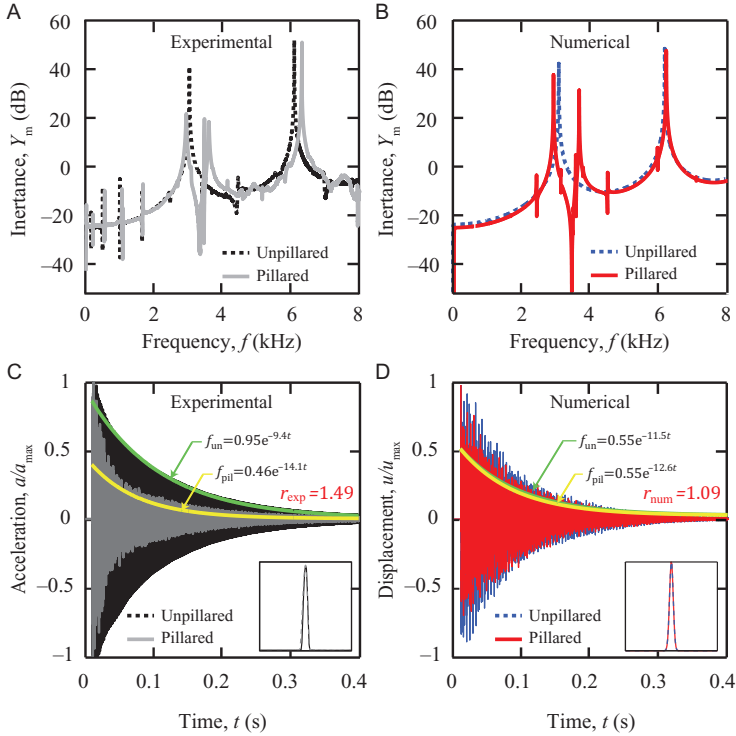


Fig. 27 (A) Experimental and (B) numerical frequency response functions for the unpillared and for the pillared beams. (C) Experimental and (D) numerical temporal responses for the two beam structures. The *green* and *yellow* curves are the curve-fitted exponential functions for the unpillared and pillared time signals, respectively, to determine their time decay rates. The form of impulse excitations are shown in the insets; these are obtained by a hammer impact in the experimental case, and mathematically synthesized in the numerical case.

model adopted, and the application of Bloch's theorem to that model, are found in Frazier and Hussein (2015) and Hussein and Frazier (2013a). The numerical FRFs (Figs. 27B) are shown to agree very well with their experimental counterparts (Fig. 27A).

8.2 Evidence of Metadamping

To determine the presence of metadamping, we seek to show that the pillared beam exhibits stronger temporal attenuation than the unpillared beam. This may be demonstrated for a finite beam by examining the temporal response due to impulse excitation, and for an infinite beam by examining the damping ratio diagram obtained from a Bloch analysis on the unit cell.

8.2.1 Finite Structure

The experimental temporal response for the same test structures investigated in Fig. 27A to a particular profile of impulse excitation is shown in Fig. 27C. To identify the presence of metadamping and quantify its intensity, we compare the rate of time decay of the pillared beam and compare it to that of the unpillared beam. The procedure is as follows. First, the first derivative of the displacement response is evaluated. Then, the maxima, which are the points where the derivative changes sign, are extracted. Exponential functions of the form $f(t) = ae^{-bt}$ are then curve-fitted to these extracted response peaks, where the exponential decay constant b provides a direct measure of the degree of dissipation.

With this approach, a metric for metadamping is defined as the ratio $r = b_{\text{pil}}/b_{\text{un}}$, where “pil” and “un” denote pillared and unpillared, respectively. A ratio greater than unity signifies positive metadamping, i.e., the time response of the pillared beam decays faster than that of the unpillared beam. Conversely, a ratio less than unity indicates negative metadamping [not covered here; see Frazier and Hussein (2015) and Bacquet and Hussein (2018)]. From the results of Fig. 27C, we report an experimental metadamping ratio $r_{\text{exp}} = 1.49$ which is indicative of nearly 50% positive metadamping, i.e., the pillared beam exhibits 50% higher dissipation than the unpillared beam for this particular form of excitation.

A similar analysis is conducted using our FE beam models by implementing a time-integration scheme particularly suited for exponentially damped systems (Adhikari & Wagner, 2004). In order to accurately replicate the experimental setup, the initial displacement is modeled as a Gaussian excitation whose parameters a and b are selected such that it matches the experimental impulse:

$$u_0(t) = e^{-\frac{(t-a)^2}{2b^2}}, \quad (50)$$

where $a = 0.01$ and $b = 8 \times 10^{-5}$. The time response of the beams are computed for $t = 0.4$ s with a time step of $\Delta t = 3 \times 10^{-5}$ s. The results, which are shown in Fig. 27D, give us a numerical metadamping ratio of $r_{\text{num}} = 1.09$. While the degree of the predicted metadamping is lower than the experimental results, this confirms that the pillared beam exhibits higher dissipation for the applied excitation profile.

8.2.2 Infinite Material

To elucidate the metadamping phenomenon, and what causes it in the finite structure as we observed by brute-force simulations, we revisit the problem

and examine it from the material point of view. This is done by performing a dispersion analysis on the unit cells (both the un-pillared and pillared) and comparing their damping ratio diagrams. The free equation of motion for each unit cell is given by Eq. (49) with the force term on the right-hand side set to zero. The dispersion band structure and corresponding damping ratio diagram are obtained by assuming a Bloch solution of the form $\mathbf{u}(t) = \tilde{\mathbf{U}}(\boldsymbol{\kappa})e^{i\boldsymbol{\kappa}\mathbf{x} + \lambda t}$ and substituting it into Eq. (49). Upon transformation to state space, we obtain the following matrix eigenvalue problem [details of the derivation are available in Hussein and Frazier (2010, 2013a) and Frazier and Hussein (2015)]:

$$\left(\lambda \begin{bmatrix} \mathbf{0} & \mathbf{M} & \mathbf{0} \\ \mathbf{M} & \mathbf{C}(\boldsymbol{\kappa}) & -\frac{1}{\mu}\mathbf{C}(\boldsymbol{\kappa}) \\ \mathbf{0} & -\frac{1}{\mu}\mathbf{C}(\boldsymbol{\kappa}) & \frac{1}{\mu^2}\mathbf{C}(\boldsymbol{\kappa}) \end{bmatrix} + \begin{bmatrix} -\mathbf{M} & \mathbf{0} & \mathbf{0} \\ \mathbf{0} & \mathbf{K}(\boldsymbol{\kappa}) & \mathbf{0} \\ \mathbf{0} & \mathbf{0} & \frac{1}{\mu}\mathbf{C}(\boldsymbol{\kappa}) \end{bmatrix} \right) \begin{bmatrix} \dot{\mathbf{u}} \\ \mathbf{u} \\ \mathbf{p} \end{bmatrix} = \mathbf{0}, \quad (51)$$

This problem is solved for prescribed and real wavenumbers $\boldsymbol{\kappa}$ spanning the first Brillouin zone ($0 \leq \boldsymbol{\kappa}a \leq \boldsymbol{\pi}$) which gives us wavenumber-dependent, complex eigenvalues $\lambda_s(\boldsymbol{\kappa})$ in the form

$$\lambda_s(\boldsymbol{\kappa}) = -\xi_s(\boldsymbol{\kappa})\omega_s(\boldsymbol{\kappa}) \pm i\omega_{ds}(\boldsymbol{\kappa}), \quad s = 1, \dots, n, \quad (52)$$

where n is the total number of modes. The imaginary part ω_{ds} represents the damped frequency corresponding to the s -th Bloch mode, and the real part is the product of the wavenumber-dependent damping ratio ξ_s and, in the case of Rayleigh (proportional) damping, the undamped frequency ω_s . The dispersion diagram for both beam structures is shown in Fig. 28A and the corresponding damping ratio diagram is plotted in Fig. 28B (we only show the relevant portions of each diagram). The latter diagram provides us with the level of dissipation that each Bloch mode exhibits.

We observe in the dispersion diagram (Fig. 28A) two curves cutting through horizontally; these represent local resonances associated with pillar motion. These curves couple with the underlying dispersion curves describing wave motion along the base beam structure and cause the hybridization phenomenon that is characteristic of locally resonant metamaterials, as we observed in the earlier sections dealing with lumped-parameter models. The pillared beam dispersion curves clearly contrast with those of un-pillared beam as the latter curves do not exhibit any local resonances. Since our earlier experimental focus has been in longitudinal displacements (and accelerations), we specifically highlight the longitudinal modes and shade the other

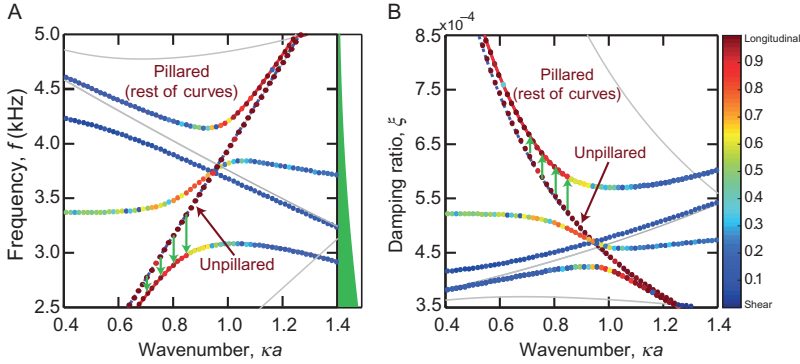


Fig. 28 (A) Dispersion and (B) damping ratio diagrams with a close-up view of the hybridization region. The green arrows illustrate the metadamping effect due to the addition of the pillars. The *color bar* represents the degree of longitudinal polarization in each mode. The frequency content of the impulse excitation is plotted and shaded in *green* on the far end of (A) demonstrating overlap with metadamping region; most of the excitation frequency content falls within the $2500 \leq f \leq 3250$ Hz range.

modes in gray. To rigorously identify which modes are longitudinal in the dispersion diagram, we first sort the Bloch modes using an algorithm that checks continuation of group velocities [which is a measure of the degree of orthogonality between two vectors (Allemang, 2003)], and then calculate the degree of longitudinal polarization following the method described in Achaoui, Khelif, Benchabane, and Laude (2010). Polarization values range from 0 (pure shear) to 1 (pure longitudinal).

The key feature in Fig. 28 is the green arrows that illustrate the transition of the dispersion curves and damping ratios due to the inclusion of the pillar in the unit cell. In the damping ratio diagram in particular, these arrows indicate an increase in the level of dissipation. And since this takes place in the frequency range of the excitation, the finite structure formed from this constituent cell experiences increased dissipation, or metadamping, as we observed in Figs. 27C and D.

8.3 Effect of Added Mass on Dissipation

Finally, it is important to ensure that the added mass of the pillar is not a factor in the generation of metadamping. The unpillared beam has a volume of $V_{\text{un}} = 32 \text{ in}^3$ whereas the pillared beam has a volume of $V_{\text{pil}} = 34 \text{ in}^3$. Therefore, to show that the metadamping is due to the local resonance

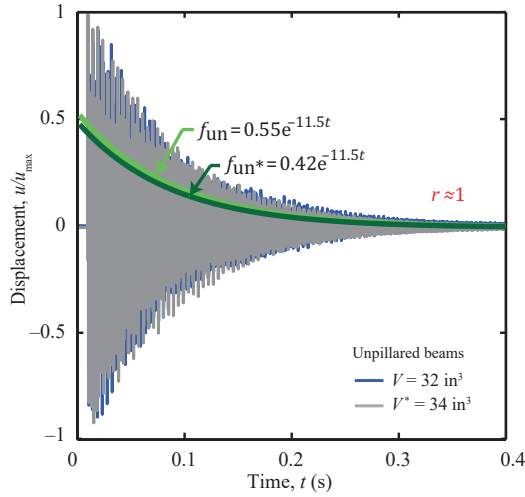
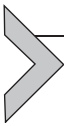


Fig. 29 Numerical time responses for the two unpillared beams, with volumes $V = 32 \text{ in}^3$ (blue) and $V^* = 34 \text{ in}^3$ (gray), respectively. The light and dark green curves correspond to exponential curves that were fitted to the unpillared and unpillared volume time signals, respectively, to determine their time decays.

phenomena only and not due to the addition of extra mass that exhibits material damping, we perform a similar analysis as that of Fig. 28D on an unpillared beam that has the same volume as the pillared beam. The numerical time responses and their curve-fitted exponential functions are shown in Fig. 29. The metadamping ratio, here redefined as $r = b_{\text{un}^*}/b_{\text{un}}$, is shown to equal one; this confirms our hypothesis that metadamping emerges from the presence of local resonance and not from the addition of more damped material.



9. CONCLUSIONS

Metadamping is a resonance-enabled intrinsic damping emergence phenomenon whereby the level of dissipation may be enhanced (or reduced) in a metamaterial compared to a statically equivalent material with the same mass and type and quantity of prescribed damping. While elastic metamaterials are known to provide strong spatial attenuation inside band gaps, metadamping enables the additional trait of strong temporal attenuation across relatively broad frequency ranges. The phenomenon takes place at regions in the wavenumber-dependent damping ratio diagram where the dissipation is shown to increase due to the inclusions of the resonances. In this chapter,

we have provided a technical review of the concept for different types of resonances, namely local dipole, local monopole, and nonlocal. It is shown that the quest for high metadamping in resonant metamaterials becomes a trade-off between seeking the absolute highest metadamping (provided by DP metamaterials) or a considerable metadamping effect across a wider choice of resonator stiffnesses (provided by NL metamaterials). A parametric study and an examination of the effects of viscous vs nonviscous damping are also provided. The chapter concludes with a real-life experimental investigation of metadamping in a pillared beam, where we show matching results with both simulations and band-structure theory. Future research may take the phenomenon of metadamping to the microscale and to waves driven at prescribed frequency.

ACKNOWLEDGMENTS

MIH acknowledges the National Science Foundation for its partial support of this work through the NSF CAREER Grant No. 1254931 and Grant No. 1538596. MIH and CLB thank Professor Srikanth Phani for fruitful discussions. MN acknowledges the National Science Foundation for its support of this work through Grant No. 1647744.

REFERENCES

- Achaoui, Y., Khelif, A., Benchabane, S., & Laude, V. (2010). Polarization state and level repulsion in two-dimensional phononic crystals and waveguides in the presence of material anisotropy. *Journal of Physics D: Applied Physics*, 43(18), 185401. <https://doi.org/10.1088/0022-3727/43/18/185401>. <http://stacks.iop.org/0022-3727/43/i=18/a=185401?key=crossref.4cfb160c209188b55ba1ab0b245fa8bd>. (updated 2017-11-17).
- Achaoui, Y., Laude, V., Benchabane, S., & Khelif, A. (2013). Local resonances in phononic crystals and in random arrangements of pillars on a surface. *Journal of Applied Physics*, 114, 104503.
- Adhikari, S., & Phani, A. S. (2009). Experimental identification of generalized proportional viscous damping matrix. *Journal of Vibration and Acoustics-Transactions of the ASME*, 131(1), 011008.
- Adhikari, S., & Wagner, N. (2004). Direct time-domain integration method for exponentially damped linear systems. *Computers & Structures*, 82(29-30), 2453-2461. <https://doi.org/10.1016/j.compstruc.2004.08.004>. <http://www.sciencedirect.com/science/article/pii/S0045794904003074>. (updated 2016-06-02).
- Al Ba'ba'a, H., DePauw, D., Singh, T., & Nouh, M. (2018). Dispersion transitions and pole-zero characteristics of finite inertially amplified acoustic metamaterials. *Journal of Applied Physics*, 123, 105106.
- Al Ba'ba'a, H., & Nouh, M. (2017). An investigation of vibrational power flow in one-dimensional dissipative phononic structures. *Journal of Vibration and Acoustics-Transactions of the ASME*, 139(2), 021003-021010.
- Al Ba'ba'a, H. B., Attarzadeh, M. A., & Nouh, M. (2017). Experimental evaluation of structural intensity in two dimensional plate-type locally resonant elastic metamaterials. *Journal of Applied Mechanics-Transactions of the ASME*, 122, 341-354.
- Al Ba'ba'a, H. B., & Nouh, M. (2017). Mechanics of longitudinal and flexural locally resonant elastic metamaterials using a structural power flow approach. *International Journal of Mechanical Sciences*, 122, 341-354.

- Allemang, R. J. (2003). The modal assurance criterion—twenty years of use and abuse. *Sound and Vibration*, 37, 14–20.
- Antoniadis, I., Chronopoulos, D., Spitas, V., & Koulocheris, D. (2015). Hyper-damping properties of a stiff and stable linear oscillator with a negative stiffness element. *Journal of Sound and Vibration*, 346, 37–52.
- Bacquet, C. L., & Hussein, M. I. (2018). *Dissipation engineering in metamaterials by localized structural dynamics*. arXiv:1809.04509 [physics.app-ph].
- Beli, D., Arruda, J. R. F., & Ruzzene, M. (2018). Wave propagation in elastic metamaterial beams and plates with interconnected resonators. *International Journal of Solids and Structures*, 139–140, 105–120.
- Bert, C. W. (1973). Material damping: An introductory review of mathematic measures and experimental technique. *Journal of Sound and Vibration*, 29(2), 129–153.
- Bilal, O. R., & Hussein, M. I. (2013). Trampoline metamaterial: Local resonance enhancement by springboards. *Applied Physics Letters*, 103(11), 111901.
- Bloch, F. (1929). Über die quantenmechanik der elektronen in kristallgittern. *Zeitschrift für Physik*, 52(7–8), 555–600.
- Brun, M., Guenneau, S., & Movchan, A. B. (2009). Achieving control of in-plane elastic waves. *Applied Physics Letters*, 94(6), 061903.
- Cassedy, E. S. (1967). Dispersion relations in time-space periodic media part II—Unstable interactions. *Proceedings of the IEEE*, 55(7), 1154–1168.
- Castanier, M. P., & Pierre, C. (1993). Individual and interactive mechanisms for localization and dissipation in a mono-coupled nearly-periodic structure. *Journal of Sound and Vibration*, 168(3), 479–505.
- Chen, Y., Hu, G., & Huang, G. (2017). A hybrid elastic metamaterial with negative mass density and tunable bending stiffness. *Journal of the Mechanics and Physics of Solids*, 105, 179–198.
- Christensen, J., Kadic, M., Kraft, O., & Wegener, M. (2015). Vibrant times for mechanical metamaterials. *MRS Communications*, 5(3), 453–462. <https://doi.org/10.1557/mrc.2015.51>.
- Collet, M., Ouisse, M., Ruzzene, M., & Ichchou, M. N. (2011). Floquet–Bloch decomposition for the computation of dispersion of two-dimensional periodic, damped mechanical systems. *International Journal of Solids and Structures*, 48(20), 2837–2848.
- Crandall, S. H. (1970). Role of damping in vibration theory. *Journal of Sound and Vibration*, 11, 3–18.
- Cummer, S. A., & Schurig, D. (2007). One path to acoustic cloaking. *New Journal of Physics*, 9(3), 45.
- DePauw, D., Al Ba'ba'a, H., & Nouh, M. (2018). Metadamping and energy dissipation enhancement via hybrid phononic resonators. *Extreme Mechanics Letters*, 18, 36–44.
- Deymier, P. A. (2013). *Acoustic metamaterials and phononic crystals*. Heidelberg: Springer, (Ed.).
- Farzbod, F., & Leamy, M. J. (2011). Analysis of Bloch's method in structures with energy dissipation. *Journal of Vibration and Acoustics-Transactions of the ASME*, 133(5), 051010.
- Floquet, G. (1883). Sur les équations différentielles linéaires à coefficients périodiques. *Annales de l'Ecole Normale Supérieure*, 12, 47–88.
- Frazier, M. J., & Hussein, M. I. (2015). Viscous-to-viscoelastic transition in phononic crystal and metamaterial band structures. *The Journal of the Acoustical Society of America*, 138(5), 3169–3180.
- Frazier, M. J., & Hussein, M. I. (2016). Generalized Bloch's theorem for viscous metamaterials: Dispersion and effective properties based on frequencies and wavenumbers that are simultaneously complex. *Comptes Rendus Physique*, 17(5), 565–577. <https://doi.org/10.1016/j.crhy.2016.02.009>.
- Hu, G., Tang, L., Das, R., Gao, S., & Liu, H. (2017). Acoustic metamaterials with coupled local resonators for broadband vibration suppression. *AIP Advances*, 7(2), 025211.

- Hussein, M. I. (2009a). Reduced Bloch mode expansion for periodic media band structure calculations. *Proceedings of the Royal Society A*, 465(2109), 2825–2848.
- Hussein, M. I. (2009). Theory of damped Bloch waves in elastic media. *Physical Review B*, 80(21), 212301.
- Hussein, M. I., Biringen, S., Bilal, O. R., & Kucala, A. (2015). Flow stabilization by subsurface phonons. *Proceedings of the Royal Society A: Mathematical, Physical and Engineering Sciences*, 471(2177), 20140928.
- Hussein, M. I., & Frazier, M. J. (2010). Band structure of phononic crystals with general damping. *Journal of Applied Physics*, 108(9), 093506.
- Hussein, M. I., & Frazier, M. J. (2013a). Damped phononic crystals and acoustic metamaterials. In P. A. Deymier (Ed.), *Acoustic metamaterials and phononic crystals* (pp. 201–215). Berlin, Heidelberg: Springer. https://doi.org/10.1007/978-3-642-31232-8_6. Chapter 6 (Ed.).
- Hussein, M. I., & Frazier, M. J. (2013b). Metadamping: An emergent phenomenon in dissipative metamaterials. *Journal of Sound and Vibration*, 332, 4767–4774.
- Hussein, M. I., Frazier, M. J., & Abedinnassab, M. H. (2013). Microdynamics of phononic materials. In S. Li & X.-L. Gao (Eds.), *Handbook of micromechanics and nanomechanics*. Pan Stanford Publishing. Chapter 1 (Eds.).
- Hussein, M. I., Leamy, M. J., & Ruzzene, M. (2014). Dynamics of phononic materials and structures: Historical origins, recent progress, and future outlook. *Applied Mechanics Reviews-Transactions of the ASME*, 66(4), 040802.
- Khajetourian, R., & Hussein, M. I. (2014). Dispersion characteristics of a nonlinear elastic metamaterial. *AIP Advances*, 4(12), 124308.
- Khelif, A., & Adibi, A. (2015). *Phononic crystals: Fundamentals and applications*. New York: Springer. (Eds.).
- Kohn, W., Krumhansl, J. A., & Lee, E. H. (1972). Variational methods for dispersion relations and elastic properties of composite materials. *Journal of Applied Mechanics-Transactions of the ASME*, 39(2), 327–336.
- Kushwaha, M. S., Halevi, P., Dobrzynski, L., & Djafari-Rouhani, B. (1993). Acoustic band structure of periodic elastic composites. *Physical Review Letters*, 71(13), 2022–2025.
- Langley, R. S. (1994a). On the forced response of one-dimensional periodic structures: Vibration localization by damping. *Journal of Sound and Vibration*, 178(3), 411–428.
- Langley, R. S. (1994b). On the forced response of one-dimensional periodic structures: Vibration localization by damping. *Journal of Sound and Vibration*, 178(3), 411–428.
- Laude, V. (2015). *Phononic crystals: Artificial crystals for sonic, acoustic and elastic waves*. Berlin: De Gruyter.
- Lee, E. H., & Yang, W. H. (1973). On waves in composite materials with periodic structure. *SIAM Journal on Applied Mathematics*, 25(3), 492–499.
- Liu, L., & Hussein, M. I. (2012). Wave motion in periodic flexural beams and characterization of the transition between Bragg scattering and local resonance. *Journal of Applied Mechanics-Transactions of the ASME*, 79(1), 011003.
- Liu, Z., Chan, C. T., & Sheng, P. (2005). Analytic model of phononic crystals with local resonances. *Physical Review B*, 71(1), 014103.
- Liu, Z., Zhang, X., Mao, Y., Zhu, Y. Y., Yang, Z., Chan, C. T., & Sheng, P. (2000). Locally resonant sonic materials. *Science*, 289(5485), 1734–1736.
- Mead, D. J. (1973). A general theory of harmonic wave propagation in linear periodic systems with multiple coupling. *Journal of Sound and Vibration*, 27(2), 235–260.
- Merheb, B., Deymier, P. A., Jain, M., Alshyha-Lesuffleur, M., Mohanty, S., Berker, A., & Greger, R. W. (2008). Elastic and viscoelastic effects in rubber/air acoustic band gap structures: A theoretical and experimental study. *Journal of Applied Physics*, 104(6), 064913.
- Moiseyenko, R. P., & Laude, V. (2011). Material loss influence on the complex band structure and group velocity in phononic crystals. *Physical Review B*, 83(6), 064301.

- Nouh, M., Aldraihem, O., & Baz, A. (2015). Wave propagation in metamaterial plates with periodic local resonances. *Journal of Sound and Vibration*, 341, 53–73. <https://doi.org/10.1016/j.jsv.2014.12.030>.
- Pendry, J. B. (2000). Negative refraction makes a perfect lens. *Physical Review Letters*, 85(18), 3966–3969.
- Pendry, J. B., Holden, A. J., Robbins, D. J., & Stewart, W. J. (1999). Magnetism from conductors and enhanced nonlinear phenomena. *IEEE Transactions Microwave Theory Techniques*, 47, 2075–2084.
- Pennek, Y., Djafari-Rouhani, B., Larabi, H., Vasseur, J. O., & Ladky-Hennion, A.-C. (2008). Low-frequency gaps in a phononic crystal constituted of cylindrical dots deposited on a thin homogeneous plate. *Physical Review B*, 78, 104105.
- Phani, A. S., & Hussein, M. I. (2013). Analysis of damped Bloch waves by the Rayleigh perturbation method. *Journal of Vibration and Acoustics-Transactions of the ASME*, 135, 041014.
- Phani, A. S., & Hussein, M. I. (2017). *Dynamics of lattice materials*. New York: Wiley.
- Phani, A. S., & Woodhouse, J. (2007). Viscous damping identification in linear vibration. *Journal of Sound and Vibration*, 303(3–5), 475–500.
- Phani, A. S., & Woodhouse, J. (2009). Experimental identification of viscous damping in linear vibration. *Journal of Sound and Vibration*, 319(3–5), 832–849.
- Russell, D. A., Titlow, J. P., & Bemmen, Y.-J. (1999). Acoustic monopoles, dipoles, and quadrupoles: An experiment revisited. *American Journal of Physics*, 67(8), 660–664.
- Sigalas, M. M., & Economou, E. N. (1992). Elastic and acoustic wave band structure. *Journal of Sound and Vibration*, 158(2), 377–382.
- Smith, D. R., Padilla, W. J., Vier, D. C., Nemat-Nasser, S. C., & Schultz, S. (2000). Composite medium with simultaneously negative permeability and permittivity. *Physical Review Letters*, 84(18), 4184–4187. <https://doi.org/10.1103/PhysRevLett.84.4184>.
- Språk, R., & Wegdam, G. H. (1998). Acoustic band gaps in composites of solids and viscous liquids. *Solid State Communications*, 106(2), 77–81.
- Sun, C. T., Achenbach, J. D., & Herrmann, G. (1968). Time-harmonic waves in a stratified medium propagating in the direction of the layering. *Journal of Applied Mechanics-Transactions of the ASME*, 35(2), 408–411.
- Wagner, N., & Adhikari, S. (2003). Symmetric state-space method for a class of nonviscously damped systems. *AIAA Journal*, 41(5), 951–956.
- Wang, G., Wen, X. S., Wen, J. H., Shao, L. H., & Liu, Y. Z. (2004). Two-dimensional locally resonant phononic crystals with binary structures. *Physical Review Letters*, 93, 154302.
- Woodhouse, J. (1998). Linear damping models for structural vibration. *Journal of Sound and Vibration*, 215(3), 547–569.
- Wu, T.-T., Huang, Z.-G., Tsai, T.-C., & Wu, T.-C. (2008). Evidence of complete band gap and resonances in a plate with periodic stubbed surface. *Applied Physics Letters*, 93(11), 111902.
- Yang, S., Page, J. H., Liu, Z., Cowan, M. L., Chan, C. T., & Sheng, P. (2004). Focusing of sound in a 3D phononic crystal. *Physical Review Letters*, 93(2), 024301.
- Zhang, X., & Liu, Z. (2004). Negative refraction of acoustic waves in two-dimensional phononic crystals. *Applied Physics Letters*, 85(2), 341–343.
- Zhang, X., Liu, Z., Mei, J., & Liu, Y. (2003). Acoustic band gaps for a two-dimensional periodic array of solid cylinders in viscous liquid. *Journal of Physics: Condensed Matter*, 15(49), 8207.